Received 21 October 2025; revised 4 December 2025; accepted 3 January 2026. Date of current version 13 January 2026.

Digital Object Identifier 10.1109/OJCOMS.2026.3651826

Towards GNSS-Free Synchronization: An Improved PSS-Based Frequency Alignment Technique for NTN

ISABEL GALLARDO-DUVAL [1,2], JOAN FRANCESC MUNOZ-MARTIN [1] (Member, IEEE), ADRIA ROVIRA-GARCIA [2] (Senior Member, IEEE), AND JOAN A. RUIZ-DE-AZUA [1,3] (Member, IEEE)

[1]Space Communications Research Group, Fundació i2CAT, 08034 Barcelona, Spain
[2]Research Group of Astronomy and Geomatics, Universitat Politècnica de Catalunya, 08034 Barcelona, Spain
[3]Department of Network Engineering, Universitat Politècnica de Catalunya, 08034 Barcelona, Spain

CORRESPONDING AUTHOR: I. GALLARDO-DUVAL (e-mail: isabel.gallardo@i2cat.net)

This work was supported in part by the Government of Catalonia in the Scope of the NewSpace Strategy for Catalonia; in part by the European Union NextGenerationEU/PRTR within the call "Ayudas Cervera para Centros Tecnológicos 2023"; and in part by the European Union's Horizon Europe under Grant 101096526 (ETHER).

ABSTRACT The growing demand for resilient positioning services has revealed the limitations of the Global Navigation Satellite System (GNSS). Furthermore, the Third Generation Partnership Project (3GPP) has advanced GNSS-free solutions within 5G and emerging 6G frameworks, with Low Earth Orbit-based Positioning, Navigation, and Timing offering lower latency and stronger signals due to satellite proximity. For synchronization, 3GPP specifies reference signals, such as the Primary Synchronization Signal (PSS) and Secondary Synchronization Signal, transmitted in Signal Synchronization Blocks (SSBs). Whereas PSS detection has been extensively studied, the impact of frequency estimation error, constrained by 3GPP 0.1 ppm carrier requirement, remains underexplored. This work evaluates the minimum Signal-to-Noise Ratio (SNR) required for synchronization in Non-Terrestrial Network bands n255 (L-band) and n256 (S-band), analyzing how transmission parameters, such as burst configuration and cyclic prefix (CP), affect detection performance. A reference detection algorithm is implemented and progressively refined. Monte Carlo simulations across realistic SNR ranges characterize its performance in terms of frequency estimation error and compliance with 3GPP specifications. The proposed implementation is also benchmarked against the ideal Cramér-Rao Lower Bound. Results show that refinements reduce frequency estimation errors by up to 36.7% with 4 SSBs and 44.9% with the full solution (combining multiple bursts, CP utilization, and algorithm refinements), whereas SNR gains reach 7 dB (10 dB) in n255 (n256), and up to 15 dB (18.3 dB) with this configuration. These results demonstrate a robust and effective synchronization strategy, supporting its potential as a viable alternative to GNSS-based positioning.

INDEX TERMS 5G, 6G, Doppler, GNSS-free, NR, NTN, PSS, SNR, synchronization.

I. INTRODUCTION

IN RECENT years, the need for global, continuous, and resilient positioning services has become essential for various commercial and industrial applications, targeting both outdoor and indoor environments [1]. This necessity has revealed limitations of traditional Global Navigation Satellite Systems (GNSS), such as weak signal propagation [2], highlighting the quest for alternatives. Moreover, the Third Generation Partnership Project (3GPP) is progressively introducing the development of GNSS-free technologies as a key aspect of its 5th Generation (5G) and 6th Generation (6G) evolution strategy [3].

As the industry shifts to 6G networks, positioning capabilities are expected to meet demanding accuracy requirements across numerous vertical and industrial applications. These applications, which represent solutions tailored to specific industry sectors, are expected to achieve cm-level accuracy and seamless service continuity [4]. In this context, Low Earth Orbit (LEO) satellites within Non-Terrestrial Networks (NTN) architectures are being explored as potential solutions due to their lower propagation delays and stronger received signal power compared to Medium Earth Orbit (MEO) and Geostationary Orbit (GEO) satellites [5], offering a promising path toward resilient, global and

GNSS-independent Positioning, Navigation, and Timing (PNT) services [2].

To facilitate positioning in cellular networks, the 3GPP introduced standardized reference signals, such as the Positioning Reference Signal (PRS). This signal is characterized by its structured pattern and configurational flexibility for determining the Time of Arrival (ToA) or Angle of Arrival (AoA) of transmissions [6]. However, before precise positioning measurements can be performed, an initial time and frequency acquisition is required to establish synchronization and enable the detection of these positioning signals.

This poses a critical challenge when GNSS is unavailable [7]. Standard NTN operations rely on GNSS data to estimate propagation delays and perform Doppler pre-compensation. Without this reference, the User Equipment (UE) is forced to depend on closed-loop controls, which are often unstable given the rapid motion of LEO satellites [7]. This absence of pre-compensation exposes the receiver to the full magnitude of the channel kinematics, resulting in a large Residual Carrier Frequency (RFO) that degrades synchronization performance. Consequently, developing robust GNSS-free synchronization methods is essential to ensure reliable initial access in GNSS-denied environments [7].

In NTN scenarios, these kinematics are characterized by high relative velocities between the UE and the satellite introduce not only significant Doppler shifts [8] (e.g., $\approx$ 46 kHz in S-band [9]) but also high Doppler rates (e.g., up to $\approx$ 580 Hz/s [9]). Maintaining synchronization becomes critical when the transmission periodicity of reference signals is large (typically ranging from 20 ms to 160 ms or longer [10]), as the frequency may vary significantly between updates. Consequently, the 3GPP synchronization performance is strongly influenced by the residual Doppler shift and rate over the synchronization interval. Large and rapidly varying Doppler causes increased Carrier Frequency Offset (CFO) and Inter-Carrier Interference (ICI), which impact the orthogonality of Orthogonal Frequency Division Multiplexing (OFDM) subcarriers and introduce additional noise [8], [9], [11].

The 3GPP defines a set of synchronization signals, such as the Primary Synchronization Signal (PSS) and the Secondary Synchronization Signal (SSS), to be used by the UE to acquire time and frequency synchronization with a cell [10] during the cell search procedure. This process begins with the detection of the PSS, which enables the UE to achieve initial coarse synchronization with the network. The accuracy of this initial synchronization directly impacts subsequent positioning operations, as residual frequency errors propagate into timing errors that degrade ranging accuracy [12], [13].

Despite its critical role, multiple studies [9], [14], [15], [16] have analyzed the probability of detecting the PSS under various channel conditions, yet often neglecting the associated frequency estimation error. This is essential to determine whether initial synchronization truly meets operational requirements. According to 3GPP specifications, the required frequency accuracy for UE operation is ± 0.1 parts per million (ppm) of the carrier frequency (3GPP TS 138.104 [17]). The present study addresses this gap by analyzing the minimum Signal-to-Noise Ratio (SNR) required to achieve initial synchronization through the detection of the PSS. To this end, the frequency error associated with PSS detection is quantified and evaluated under 3GPP specifications.

The analysis conducted in this work focuses on two NTN frequency bands standardized by the 3GPP: n255 (L-band) and n256 (S-band) [18], which are the bands planned for mobile-to-space communication. Furthermore, the study examines the impact of critical transmission parameters on synchronization performance, including the number of Synchronization Signal (SS) bursts, the number of Synchronization Signal Block (SSB)s per SS burst, and the use of the Cyclic Prefix (CP) in the estimation algorithm. A conventionally used algorithm for PSS detection is implemented as a reference, and several enhancements are progressively introduced to improve frequency estimation accuracy, including a refining frequency offset stage. Through Monte Carlo simulations, the performance of the algorithm and the proposed enhancements are characterized in terms of frequency estimation error, complying with 3GPP accuracy requirements across realistic SNR operating ranges for LEO-based NTN scenarios.

In summary, the key contributions of this paper are: (a) Quantification of the frequency estimation error associated with the 5G New Radio (NR) PSS detection; (b) Definition of the minimum SNR required for achieving synchronization in a NTN context; (c) Analysis of the impact on accuracy of the number of SS bursts and the number of SSBs per SS burst; (d) Analysis of the impact on accuracy of the use of the CP in the estimation algorithm; (e) Design of progressive enhancements to improve accuracy for PSS detection, and (f) Demonstration through Monte Carlo simulations of the proposed enhancements.

The remainder of the paper is organized as follows. Section II reviews related work on PSS detection. Section III describes the materials and methods, including the 5G frame structure, correlation-based detection techniques, and the employed methodology. Section IV presents the reference algorithm and the proposed improvements. Section V details the simulation setup, evaluation metrics, and link budget definition. Section VI reports and analyzes the results, whereas Section VII discusses practical implementation aspects. Finally, Section VIII summarizes the findings and concludes the paper.

II. STATE OF THE ART

Accurate synchronization through PSS detection is fundamental for leveraging 5G NR signals in positioning applications. This section reviews existing research on PSS detection, with an emphasis on frequency offset estimation, and identifies research gaps in both Terrestrial Networks (TN) and NTN contexts.

Previous research on PSS detection has addressed sector index identification, Integer Frequency Offset (IFO) estimation, and Fractional Frequency Offset (FFO) recovery. The sector index, typically referred to as the Physical Layer Cell ID (PCI), uniquely identifies a sector of a next generation Node-B (gNB) [19]. The IFO and the FFO compose the CFO. The IFO corresponds to the integer part of the CFO, and the FFO corresponds to the fractional part of the CFO, both normalized by the Subcarrier Spacing (SCS) [16], [20], which refers to the frequency difference between adjacent subcarriers in an OFDM system [21]. These components induce subcarrier shifts in the frequency domain and are typically estimated and compensated separately due to computational convenience [20]. Several studies [20], [22], [23] have proposed algorithms that leverage the symmetric properties of the PSS to enable effective IFO estimation. In addition, CP-based techniques, such as the method described in [24], have been employed to estimate the FFO and perform coarse timing adjustments.

The majority of research on PSS detection has focused on TN scenarios, where channel conditions are relatively stable and Doppler shifts remain moderate. You and Song [14] designed an IFO and PSS detection scheme for 5G-NR systems, cross-correlating the received signal with three shifted versions of the locally generated PSS sequence. Their detector achieved efficient detection within a SNR range of 2 to 8 dB in TN contexts, with performance evaluated through theoretically-derived detection failure probabilities. However, the residual frequency error after synchronization was not quantified.

Yan and Tian [16] proposed a frequency-domain approach for PSS detection incorporating pre-frequency offset compensation, fast convolution, and overlap-add methods. Following a similar strategy as in [14], the received signal was cross-correlated with three local sets of the PSS. The study demonstrated successful detection at notably low SNR values, particularly around –3 dB. Despite this advancement, the frequency estimation error was not quantified. Stevens and Younis [15] developed an Long Term Evolution (LTE) PSS cell detector for airborne applications based on optimized threshold implementation tailored for Zadoff-Chu sequences. Effective detection was achieved even at around –7 dB. However, the frequency error remained unquantified.

These TN studies demonstrate reliable detection even at negative SNR values. However, frequency estimation accuracy has been systematically overlooked. Whereas detection probability indicates whether a signal can be identified, it does not address whether the synchronization is sufficiently accurate for positioning operations. Furthermore, the application of PSS detection in NTN is still an emerging area of research. Compared to TN, NTN scenarios present significantly higher Doppler shifts due to satellite motion, larger propagation delays, and time-varying channel characteristics from orbital dynamics [5], imposing more demanding implementations to meet synchronization requirements.

Considering an NTN scenario, Meshram et al. [8] proposed a technique for UEs at overlapping spot beam edges, jointly estimating both IFO and FFO. The received signal was cross-correlated with an aggregated reference PSS, complemented by CP-based FFO refinement. However, the reported performance revealed a Root Mean Square Error (RMSE) of FFO estimation of 0.1 (normalized to a SCS of 30 kHz), corresponding to 3000 Hz absolute error. At an operating frequency of 2.2 GHz, this corresponds approximately to 1.36 ppm, significantly higher than the 3GPP requirement of 0.1 ppm accuracy. Tuninato and Garello [9] designed a PSS detector for handheld UEs in L-band and S-band, incorporating adaptive SSB structure modification based on an analytical model that explicitly accounts for ICI effects from high Doppler shifts. Their results demonstrated detection capability at –4 dB and –6 dB, representative of satellite-to-handheld links. However, the accuracy of frequency estimation was not evaluated, leaving open whether their implementation meets 3GPP specifications.

Yoneda et al. [25] investigated PCI detection probability under large CFO for 5G-NR TN and NTN at mm-wave frequencies, where proportionally larger absolute frequency offsets increase synchronization challenges. Their two-stage method implemented CP-based FFO estimation followed by correlation-based IFO estimation, achieving efficient detection between an SNR of –4 dB and 0 dB. In line with the TN literature, the frequency error associated with the detection was not quantified.

Overall, the studies have addressed the detection probability that can be achieved and the associated SNR range, but the frequency estimation error has remained unquantified for most of them. This is relevant considering that merely detecting the signal may not suffice for a PNT application. 5G NR aims to support use cases like autonomous driving and industrial automation where sub-meter accuracy and precise timing are critical [12]. The present work addresses this gap by jointly characterizing PSS detection performance and frequency estimation accuracy in LEO NTN contexts, explicitly benchmarked against 3GPP specifications, establishing the operational feasibility of using NTN synchronization signals for positioning applications.

III. BACKGROUND

The present work addresses the detection of a 5G signal, in particular the PSS, for PNT purposes. Therefore, this section explores the structure of 5G signals, including the definition of the SSB and the 3GPP standardized SS burst.

A. 5G FRAME

The 5G frame is the fundamental unit of time and frequency for resource allocation in the NR downlink, uplink, and sidelink transmissions. The structure consists of a slot and symbol-based design, which enables flexible and dynamic adjustment to different service requirements such as low

latency, ultra-high bandwidth, and high connection density [26]. This is possible as the 5G frame utilizes a multi-carrier modulation system, the OFDM, that divides the available frequency spectrum into multiple orthogonal subcarriers. To support these capabilities, dedicated channels for both control and data transmission exist [19]. For control channels, three main types are defined: (1) the Physical Downlink Control Channel (PDCCH), for downlink control information, scheduling, and resource allocation purposes, (2) the Physical Uplink Control Channel (PUCCH), for uplink control information, and (3) the Physical Broadcast Channel (PBCH), for broadcast system information, essential for initial access procedures. Similarly, for data transmission, two channels are defined: (1) the Physical Downlink Shared Channel (PDSCH), for downlink user data, and (2) the Physical Uplink Shared Channel (PUSCH), for uplink user data.

Note that, similar to the PSS, the Demodulation Reference Signal (DMRS) is used for decoding both the PDSCH and the PUSCH [19], as the UE relies on it to estimate the radio channel conditions necessary for demodulating data. Moreover, the 3GPP-standardized PRS is specifically designed for high-accuracy positioning [27] and, if properly configured (e.g., utilizing wider bandwidth and longer duration [28]), yields superior precision compared to the PSS. However, the PRS implies a search space of 4096 possible Identifications (IDs) [28], and its configuration must be extracted from system information, a process that fundamentally requires prior detection of the PSS. Furthermore, the sparser periodicity of the PRS (typically $\geq$ 160 ms [10]) makes it insufficient for tracking high Doppler rates in LEO compared to the standard 20 ms periodicity of the PSS [10]. Regarding the SSS, although it shares the temporal density of the PSS, it presents 336 possible IDs [10], making a brute-force search under high Doppler uncertainty computationally infeasible without first detecting the PSS. In the present work, only the PSS is considered for detection, since the DMRS is sent exclusively during data transmission, while the SSS and PRS are unsuitable for initial acquisition due to their large search space and, in the case of the PRS, insufficient temporal density. In addition, the SSB serves as the initial signal for cell acquisition, with the PSS always positioned first within the SSB, reflecting its prerequisite role in achieving initial synchronization.

The 5G frame duration is fixed to 10 ms, comprising 10 sub-frames of 1 ms [19]. Each sub-frame contains a variable number of slots, depending on the SCS (Δf), which is the distance between adjacent subcarriers in an OFDM signal. It can range from 15 to 960 kHz, impacting the frequency spectrum occupied by the signal. The SCS is defined through the so-called numerology (μ), a concept which describes multiple waveform parameters, such as the SCS, the slot length, and the symbol duration. The 5G numerology ranges from 0 to 6. The mathematical definition of the SCS (indicated as Δf) is presented in (1). The SCS increases exponentially with the parameter μ, scaled from a base value of 15 kHz (the SCS in LTE), and $\mu = \{0, 1, 2, 3, 4, 5, 6\}$. All these cases are listed in Table 1.

TABLE 1. Subcarrier spacing as a function of numerology (μ). Adapted from 3GPP TS 38.211 [19].

μ	0	1	2	3	4	5	6
SCS (kHz)	15	30	60	120	240	480	960

$$\Delta f = 2^{\mu} \cdot 15 \text{ kHz} \tag{1}$$

Whereas the numerology impacts the slot length and symbol duration, the number of OFDM symbols per slot is fixed according to the CP. The CP is used as a guard interval between OFDM symbols, mitigating Inter-Symbol Interference (ISI) and timing errors. Currently, the 3GPP defines two types of CP: normal (14 OFDM symbols per slot) and extended (12 OFDM symbols per slot). The extended CP uses fewer OFDM symbols per slot due to its longer symbol duration. The extended CP is useful for environments with high delay spreads [29]. However, the extended CP is not supported for all numerologies, only for $\mu = 2$, which the 3GPP establishes is only supported for data transmission, not synchronization [19]. Moreover, the 3GPP provides predefined symbol configurations according to the slot format, which is categorized into uplink, downlink, or flexible (allowing for switching between both uplink and downlink) (3GPP TS 38.213 [10]).

Transmissions are represented in the time and frequency domains using the 5G NR resource grid, which is composed of two dimensions: frequency in the vertical axis, divided into subcarriers, and time in the horizontal axis, divided into OFDM symbols. Each resource grid is defined for a given antenna port, numerology, and transmission direction (downlink or uplink) [19]. Every cell of this grid is called a Resource Element (RE), the smallest physical resource unit in NR. The RE is uniquely identified by (k, l), where k is the frequency domain index, indicating the subcarrier, and l is the OFDM symbol position in the time domain. In addition, the 3GPP defines a Resource Block (RB) as 12 consecutive subcarriers in the frequency domain [19]. Fig. 1 shows the resource grid and its fundamental components: RB and the RE.

B. 5G SYNCHRONIZATION SIGNALS

The 5G-NR is characterized by its flexible resource allocation. However, synchronization in both time and frequency domains remains a critical aspect in NTN as the OFDM signal is highly sensitive to timing and frequency errors [7]. To acquire time and frequency synchronization with a cell, a UE must perform the cell-search procedure [10]. For this purpose, the UE receives two synchronization signals, the PSS and the SSS. These signals are used to detect the PCI of the cell, which is derived from (2), and ranges between 0 and 1007. Based on the SSS, the $N_{\text{ID}}^{(1)}$ is obtained, which represents the identity group and ranges from 0 to 335 ($N_{\text{ID}}^{(1)} \in \{0, 1, \ldots, 335\}$). The PSS provides the $N_{\text{ID}}^{(2)}$, which

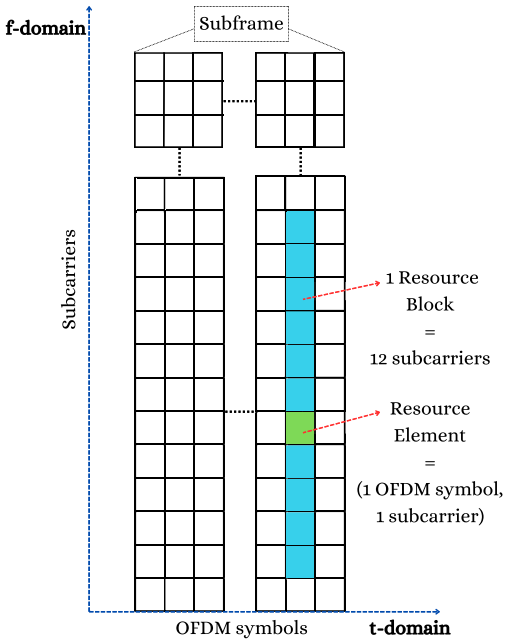

FIGURE 1. The 5G NR resource grid, illustrating its fundamental components (RB and RE) across the time (horizontal axis) and frequency (vertical axis) domains.

is the identity within the group that ranges between 0 and 2 ($N_{\mathrm{ID}}^{(2)} \in \{0, 1, 2\}$). The PSS is based on a Binary Phase-Shift Keying (BPSK) modulated m-sequence, whereas the SSS is based on a BPSK modulated Gold sequence. The details of the definition of both sequences can be found in 3GPP TS 38.211 [19].

$$N_{\mathrm{ID}}^{\mathrm{cell}} = 3N_{\mathrm{ID}}^{(1)} + N_{\mathrm{ID}}^{(2)} \tag{2}$$

C. SYNCHRONIZATION SIGNAL BLOCK

The SSB is an essential element of the 5G NR synchronization process. SSBs are periodically transmitted by gNBs and detected by UEs, enabling synchronization. The SSB comprises the PSS, the SSS, and the PBCH, which carries the Master Information Block (MIB). Regarding the structure, it occupies 240 consecutive subcarriers in the frequency domain (from $k = 0$ to $k = 239$), and spans over 4 OFDM symbols in the time domain (from $l = 0$ to $l = 3$). Each element of the SSB is always received on a specific OFDM symbol, which is detailed in Table 2. Both the PSS and SSS occupy 127 subcarriers and a single symbol, the first and the third, respectively. On the other hand, the PBCH spans from the second to the fourth symbol, and occupies 240 subcarriers. Apart from the second symbol, where the PBCH occupies 96 subcarriers. This distribution is represented in Fig. 2.

The 3GPP standard enables the transmission of SSBs in SS bursts, typically with a periodicity of 20 ms. However, it can vary according to the application, with supported periodicities of 5 ms, 10 ms, 20 ms, 40 ms, and 160 ms [10]. Note that the algorithm proposed in the present study is supported by this capability of multiple SSB transmissions.

TABLE 2. Allocation of the SSB components in the time-frequency domain, defined by OFDM symbols (l) and subcarriers (k). Adapted from 3GPP TS 38.211 [19].

Channel/Signal	OFDM symbol number l	Subcarrier number k
PSS	0	56,...,182
SSS	2	56,...,182
Set to 0	0	0,...,55, 183,...,239
	2	48,...,55, 183,...,191
PBCH	1,3	0,...,239
	2	0,...,47, 192,...,239
DMRS	1,3	0+ν,4+ν,8+ν,...,236+ν
	2	0+ν,4+ν,8+ν,...,44+ν 192+ν,196+ν,...,236+ν

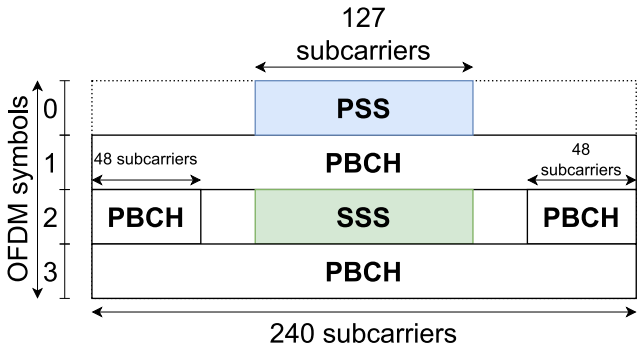

FIGURE 2. Structure of the SSB, showing the distribution of the PSS, SSS, and PBCH across subcarriers and OFDM symbols.

The maximum number of SSBs per SS burst (L_{max}) depends on the carrier frequency: up to 3 GHz, $L_{max} = 4$; between 3 GHz and 6 GHz, $L_{max} = 8$; and for frequencies above 6 GHz, $L_{max} = 64$. This feature is primarily intended for terrestrial gNBs equipped with multiple beams, allowing the transmission of multiple SSBs in up to eight spatial directions.

IV. DETECTING THE 5G-NR PSS

The present study quantifies the frequency error associated with detecting the 5G-NR PSS according to 3GPP requirements, aiming to achieve synchronization. For this purpose, a conventionally used method in literature for synchronization involving the PSS detection [8], [21], [30] is implemented. This algorithm is composed of two stages: first, a coarse search to estimate and compensate for the IFO and the time delay; and second, a fine search to estimate and compensate for the FFO. This process is depicted in Fig. 3. For clarity, this algorithm is referred to as the *reference algorithm* throughout the present contribution.

Note that the PSS is contained in an SSB, which is transmitted in bursts. The received signal is introduced in the tracking loops in segments, each corresponding to an SS burst, which are subsequently non-coherently integrated. This is proposed to process the SS bursts jointly to improve the detection performance. Non-coherent integration is based on removing the phase variations by adding up the squared magnitude [31]. Since the PSS presents random phases, non-coherent integration is usually used for its detection [21].

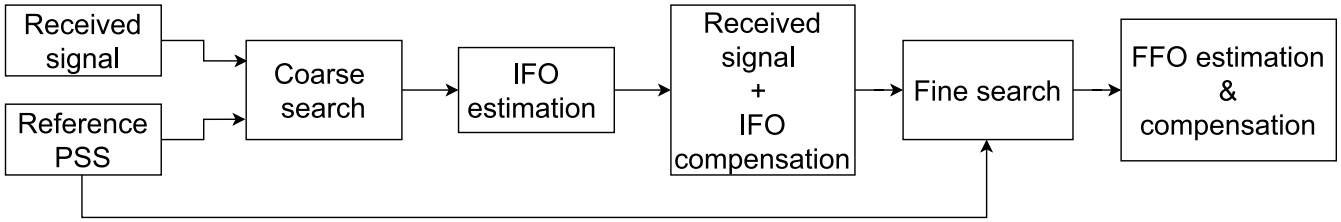

FIGURE 3. Reference PSS detection algorithm for the estimation and compensation of IFO and FFO, using coarse and fine search stages respectively.

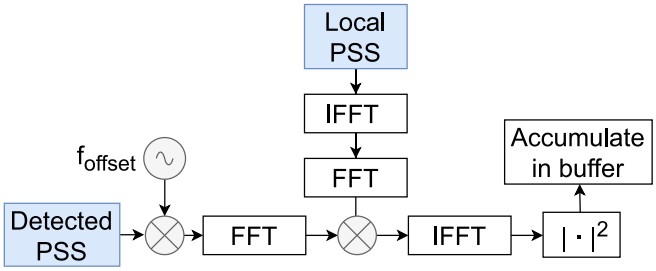

FIGURE 4. Circular correlation scheme (Coarse search for IFO estimation).

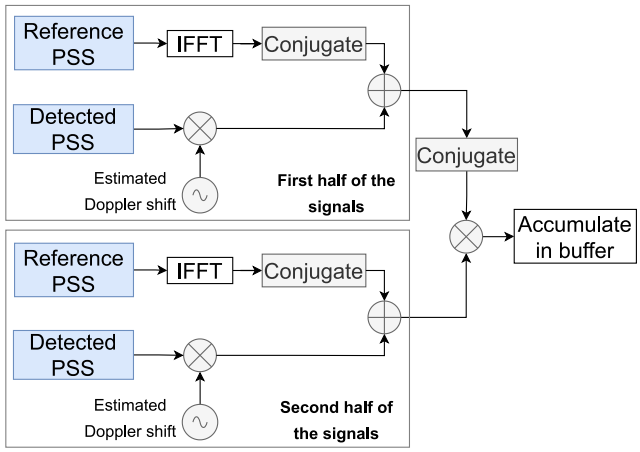

FIGURE 5. Autocorrelation scheme (Fine search for FFO estimation).

Regarding the IFO and time-delay estimation, the coarse search is performed by evaluating a grid of tentative Doppler frequency shifts. For each frequency hypothesis, the received signal is compensated and correlated with the local PSS. This is implemented via circular correlation using a parallel Fast Fourier Transform (FFT) architecture to efficiently search the time domain, as in [32]. This scheme is presented in Fig. 4. The frequency-compensated signal undergoes an FFT transformation. The result is multiplied point-wise with the frequency-domain representation of the local PSS (the reference sequence used to estimate the frequency offset). The result is converted to the time domain by implementing the Inverse Fast Fourier Transform (IFFT), and the magnitude-squared operation is applied to obtain the correlation peak, where the peak index determines the estimated time delay. After compensating for the IFO, the FFO is estimated by implementing a split-symbol correlation (often referred to as autocorrelation in synchronization contexts), as in [21]. This fine search exploits the good correlation properties of the M-sequences that form the PSS [21]. Specifically, the detected PSS (time-domain) is divided into two segments of equal length (corresponding to half the symbol size). Each segment is correlated independently with the corresponding segment of the local reference PSS. This scheme is presented in Fig. 5. Before correlation, each branch applies Doppler shift compensation using the estimated IFO. The outputs of the two segments are multiplied (conjugate of the first times the second) to extract the phase rotation between the first and second half symbol, which is proportional to the residual frequency error. Finally, the resulting complex values are averaged over the integration period.

Note that the impact of timing uncertainty, a dominant impairment in NTN initial access [7], [33], is mitigated in the present architecture through the joint time-frequency grid in the coarse search. By identifying the global maximum of the cross-correlation function across the search window, the algorithm inherently resolves the large timing uncertainty before frequency refinement. Furthermore, the subsequent fine-frequency estimation is robust against residual timing errors. Since a timing offset primarily reduces the correlation magnitude rather than distorting the phase information used for frequency estimation, the accuracy is preserved provided the timing error remains within the correlation peak.

A. ALGORITHM IMPROVEMENTS

The current study proposes two improvements to the reference detection algorithm: first, including the CP of the signal in the correlations; and second, adding a refining frequency offset stage.

1) USE OF CYCLIC PREFIX

In the literature, the CP is commonly excluded from the correlations [16], [34], even though it can be used to achieve coarse synchronization before detecting the PSS [21], [22], [35]. The present study proposes the inclusion of the CP in the tracking loop by adding it to the IFFT block of the algorithms. This inclusion aims to improve signal correlation by enhancing the processing gain when implementing longer sequences [36].

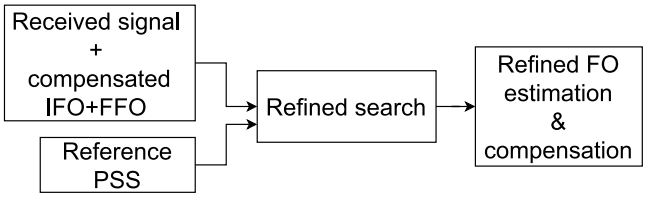

FIGURE 6. The proposed enhanced PSS detection algorithm, which introduces a refined search stage to correct the residual frequency offset remaining after standard IFO and FFO compensation.

2) REFINING FREQUENCY OFFSET STAGE

The implementation of frequency offset refining aims to improve the accuracy of Doppler estimation. After compensating for the IFO and FFO, a second circular correlation with a reduced search space is performed. This scheme is presented in Fig. 6. This algorithm will be referred to as the *enhanced algorithm* throughout this study. Note that the enhanced connotation refers to an enhancement in terms of estimation accuracy. In terms of computational cost, the enhanced algorithm presents a higher cost. Both algorithms exhibit the same asymptotic computational complexity of $O(N \times M)$ [37], N representing the received signal length and M the reference signal length. However, the enhanced algorithm implements a three-stage detection, increasing the cost of processing time at the expense of increasing accuracy.

V. PSS SIGNAL DETECTION SIMULATION

To evaluate the frequency error associated with the detection of the PSS detection algorithm and its enhancements, a Monte Carlo simulation under varying SNR conditions is performed.

A. SCENARIO

The scenario considered models an NTN downlink channel from a full gNB regenerative payload in a satellite to a mobile device on the ground, representative of a Direct-to-Cell service. It is assumed that the UE is equipped with a receiver capable of processing 5G NR downlink signals. It is also assumed that the downlink is dedicated and free from frequency interference, allowing an isolated analysis of the detection process.

In terms of the configuration of the simulated 5G signal, this study implements $\mu = 1$, corresponding to an SCS of 30 kHz. For S-band, the SCSs available are 15 kHz, 30 kHz, and 60 kHz [38]. In LEO scenarios within this band, Doppler shifts can reach approximately $\pm$ 46 kHz [9], potentially exceeding the SCS. While larger SCS (e.g., 60 kHz) would naturally exhibit higher robustness to ICI [39], it would also reduce the CP duration [19], negatively impacting robustness against delay spread. Therefore, 30 kHz is selected as a trade-off. Fig. 8 shows the slot structure and SSB distribution for the proposed configuration ($\mu = 1$ and normal CP). Moreover, an FFT size of 256 samples is used to generate the time-domain waveform (because it provides a higher

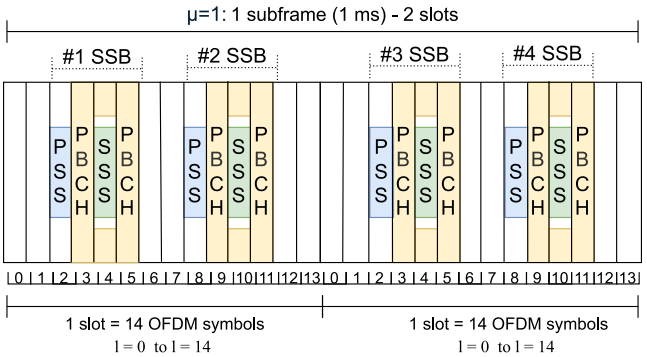

FIGURE 7. SSB distribution for $\mu = 1$ (SCS = 30 kHz) and normal CP.

TABLE 3. Summary of the main 5G signal parameters, including frame structure, bandwidth specifications, and Doppler model.

Parameter	Value
μ	1
SCS	30 kHz
FFT size	256 samples
CP lenght	7% of FFT size
Symbols	28 OFDM symbols
Sampling rate	7.68 MHz
BW	7.2 MHz
Doppler shift	$\pm$46 kHz
Doppler rate	580 Hz/s

PSS detection probability [40]), which consists of 28 OFDM symbols. By observing Fig. 7, this covers a total of four SSBs (the maximum allowable for S-band according to 3GPP specifications), which are all transmitted within a single SS burst. Both the PSS and SSS are inserted at their predefined positions according to the 3GPP SS burst structure. Note that when implementing the CP, this is added to each OFDM symbol according to a pre-defined length, which is often set to 7% of the FFT size [41]. Moreover, the sampling rate is set to 7.68 MHz, and the total bandwidth (BW) occupied by the SS burst is 7.2 MHz. This is given by (3), where $\#f_k$ corresponds to the number of subcarriers (240 in the 5G SSB), and Δf is the SCS of 30 kHz.

$$\mathrm{BW} = \#f \cdot \Delta f \tag{3}$$

Furthermore, the simulated channel incorporates Doppler effects. The initial Doppler shift is drawn from a uniform distribution within $\pm$46 kHz, while the Doppler rate is fixed at 580 Hz/s. As reported in [9], this rate corresponds to the maximum value at zenith for an S-band satellite at an altitude of 600 km. The time evolution of the Doppler shift (f_D) between SS bursts is modeled linearly [8], [42], as shown in (4). Here, $f_D(t_0)$ represents the initial shift sampled at t_0, $\dot{f}_D$ denotes the Doppler rate, and Δt_{SSB} is the standard SS burst periodicity (20 ms). In summary, all these parameters have been listed in Table 3.

$$f_D = f_D(t_0) + \dot{f}_D \cdot \Delta t_{SSB} \tag{4}$$

B. EVALUATION METRICS

The present work quantifies the frequency estimation error according to the integration time, which is directly translated into the number of SS bursts integrated (based on the 3GPP standard burst periodicity of 20 ms). This has been performed by computing the Allan Deviation (ADEV) of the measurements and the integration time associated. Moreover, the frequency estimation error obtained is compared against the theoretical Cramer-Rao Lower Bound (CRLB).

1) ALLAN DEVIATION

The ADEV is defined as the square root of the Allan variance and is commonly used to characterize frequency stability in clocks, oscillators, and amplifiers [43]. Both quantities are given in (5) (from [43]), where $\sigma_y(\tau)$ denotes the ADEV and $\sigma^2 y(\tau)$ the Allan variance. In this definition, τ is the integration time, which specifies the interval over which the measurements are averaged; y represents the fractional frequency deviation; and $(x_{n+2} - 2x_{n+1} + x_n)^2$ corresponds to the squared second finite difference of the time (or phase) measurements, which captures fluctuations in the oscillator frequency between consecutive intervals.

$$\begin{cases} \sigma_y(\tau) = \sqrt{\sigma_y^2(\tau)} \\ \sigma_y^2(\tau) = \frac{1}{2\tau^2}\left\langle (x_{n+2} - 2x_{n+1} + x_n)^2 \right\rangle \end{cases} \tag{5}$$

2) CRAMÉR-RAO LOWER BOUND

The performance of a frequency estimator is often assessed through the CRLB [44], which establishes the theoretical lower bound on the variance of an unbiased estimator [45]. This bound characterizes the best achievable accuracy of the estimator. In this study, the CRLB for PSS detection is given in (6), where $var(\hat{\Delta f})$ denotes the estimator variance, SNR is the SNR of the transmission, T_s the sampling period and N the number of samples. A detailed derivation of this expression is provided in Appendix B.

$$var\left(\hat{\Delta f}\right) \geq \frac{3}{(2\pi)^2 \cdot SNR \cdot T_s^2 \cdot N(N-1)(2N-1)} \tag{6}$$

The CRLB for a single SSB (var_1) is represented using (6), corresponding to an integration time of $\tau = 20$ ms. To find the CRLB when integrating over M independent SSBs, the variance is reduced by a factor of M, as established in standard statistical theory [45]. This reduction arises because the integration is non-coherent, where phase information is not accumulated, implying that the estimation is performed on independent symbols. This leads to the expression in (7).

$$\mathrm{var_M} = \frac{\mathrm{var_1}}{M} \tag{7}$$

Furthermore, in an NTN context, estimation accuracy is compromised by Doppler shifts resulting from the orbital dynamics of LEO satellites [5]. Consequently, the impact of the Doppler rate must be accounted for. In the present study, the Doppler rate ($\dot{f}_D$) introduces a linear frequency drift.

TABLE 4. Summary of simulation combinations, where: ***No.*** is the assigned number; ***Algorithm*** indicates the algorithm used (reference or enhanced); ***#SSB*** is the number of integrated SSBs; and ***CP*** specifies if the CP is included (w/) or not (w/o).

No.	Algorithm	# SSB	CP
1	Reference	1 SSB	w/o CP.
2	Reference	1 SSB	w/ CP.
3	Reference	4 SSB	w/o CP.
4	Reference	4 SSB	w/ CP.
5	Enhanced	1 SSB	w/o CP.
6	Enhanced	1 SSB	w/ CP.
7	Enhanced	4 SSB	w/o CP.
8	Enhanced	4 SSB	w/ CP.

Since the estimator averages the frequency over the total integration time (T_{int}), a systematic bias (f_{off}) arises relative to the start of the integration. This is quantified in (8), where Δt_{SSB} corresponds to the standard SS burst periodicity, and M denotes the number of integrated SSBs.

$$\begin{cases} f_{off} = \dot{f}_D \cdot \frac{T_{int}}{2} \\ T_{int} = \Delta t_{SSB} \cdot M \end{cases} \tag{8}$$

The definition of the CRLB is intended to serve as a benchmark for the results obtained from the ADEV computation. While accounting for both random noise (var_M) and systematic bias (f_{off}) yields the total Mean Square Error (MSE) for M integrated SSBs, defined in 9. The ADEV represents a deviation metric. Therefore, to ensure a comparable scale, the corresponding RMSE_{CRLB} (indicated as RMSE_M) is computed as presented in (10).

$$\mathrm{MSE}_M = \mathrm{var}_M + f_{off}^2 \tag{9}$$

$$\mathrm{RMSE}_M = \sqrt{\mathrm{MSE}_M} = \sqrt{\frac{\mathrm{var_1}}{M} + \left(\dot{f}_D \cdot \frac{Tint}{2}\right)^2} \tag{10}$$

C. SIMULATION SETUP

For the execution of the simulations, the baseline case has been defined as the reference PSS detection algorithm, considering the transmission of a single SSB within the SS burst. Based on this, the impact of the following three elements has been explored: first, the impact of integrating 4 SSBs instead of 1 SSB; second, the impact of adding the CP when performing the signal correlation; and third, the impact of implementing the enhanced algorithm. This results in a total of eight combinations; for clarity, these are listed in Table 4. Throughout the study, this nomenclature will be used to refer to them. *No.* indicates the number assigned to each case, *Algorithm* differentiates between reference and enhanced, *# SSB* shows the number of SSBs integrated, and *CP* indicates whether the CP is included (w/) or not (w/o). Only cases No. 1, No. 2, No. 3, No. 5, and No. 8 were considered relevant for analysis, as they illustrate the impact of the elements under investigation. The remaining cases were simulated but are not discussed in the present study.

The simulation consisted of executing 100 Monte Carlo trials. This number was considered sufficient, as results

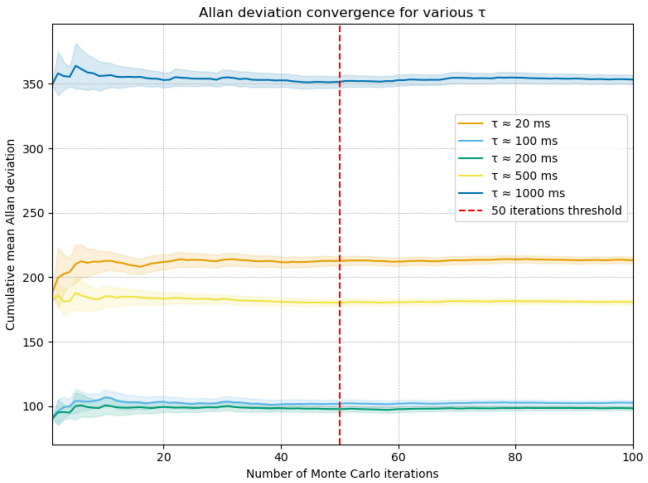

FIGURE 8. Cumulative mean ADEV as a function of the number of Monte Carlo iterations. The vertical axis shows the ADEV, whereas the horizontal axis represents the iteration number. Each colored line corresponds to a different averaging time, τ. The vertical dashed red line indicates the 50-iteration threshold.

with 50 and 100 trials showed similar frequency error trends across SNR levels. Fig. 8 illustrates this comparison through the cumulative mean ADEV [46] for integration times τ ranging from 20 ms to 1 s. The vertical axis shows the cumulative mean ADEV, whereas the horizontal axis indicates the number of trials. Distinct colors represent different τ values, the dashed vertical line indicates the 50-iteration threshold, and the shaded regions denote the 95% confidence interval (CI) [46]. After approximately 20 trials, the mean stabilizes and the CI narrows, confirming statistical reliability.

Each simulation trial consisted of generating a received signal at a specified SNR level. The signal was impaired by Additive White Gaussian Noise (AWGN), a common noise model for the NTN channel [47], and the Doppler effects were incorporated as detailed in Section V-A. The detection algorithm is then applied to estimate the frequency offset across different noise levels. The total frequency offset equals the sum of the applied corrections: IFO, FFO, and, when used, the refined frequency offset. In terms of the total integration time, at each trial, 4 seconds of signal are processed. This can be translated into a total of 200 SS bursts according to the standard burst periodicity of 20 ms. This duration is acceptable given a Doppler rate of 580 Hz/s [9], leading to a 2.32 kHz frequency deviation over 4 s, sufficient for the intended LEO-NTN application.

Regarding the configuration of the algorithm, the coarse search space was set to ±60 kHz with 15 kHz steps, selected to ensure coverage of the maximum expected Doppler shift ($\approx \pm 46$ kHz) plus a safety margin. The step size was chosen to guarantee that the maximum residual error, corresponding to half the step size (±7.5 kHz), remains within the search space of the subsequent stage. The fine search space was set to ±15 kHz, corresponding to half of the SCS (30 kHz), as conventional PSS detection is typically limited to offsets smaller than half the subcarrier interval [48]. Finally, the additional fine search space of the enhanced algorithm was set to ±1 kHz with 50 Hz steps, performing a high-precision local search to further minimize the residual error. This information is summarized in Table 5.

TABLE 5. Search space configuration for the coarse, fine, and refined searches.

Stage	Search space
Coarse search (IFO)	±60 kHz with 15 kHz steps
Fine search (FFO)	±15 kHz
Refined search	±1 kHz with 50 Hz steps

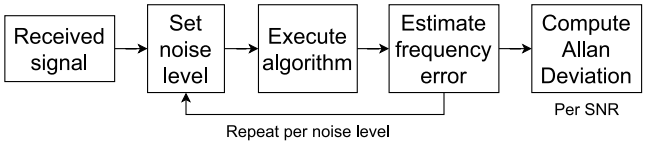

FIGURE 9. Flow diagram of the Monte Carlo simulation.

The simulations have been executed in Python, and the ADEV of the frequency error has been computed using the AllanTools Python package [49]. Starting from the frequency error provided by the algorithm, two main parameters are obtained: (1) the ADEV (σ_y) and (2) the integration time (τ). The results provide the evolution of the frequency error variation over time for different SNR values. The ADEV determines how the frequency varies, similar to the standard deviation of a normal distribution. Note that the resulting error represents approximately 68% of values that are within $\pm\sigma_y$. To clarify the simulation process, Fig. 9 shows the steps followed.

The resulting accuracy has been analyzed based on the 3GPP requirement of 0.1 ppm of the carrier frequency. To ensure compliance across the entire band, the most restrictive frequency for both uplink and downlink has been selected, since the allowed error margin scales with the carrier frequency. Specifically, 1525 MHz (152 Hz as the reference) has been considered for n255, and 1980 MHz (198 Hz as the reference) for n256. By adopting the most restrictive case, it is guaranteed that the proposed solution meets the 3GPP requirement throughout the complete operating range of each band. Furthermore, this study provides the minimum SNR conditions required to fulfill this requirement for both NTN frequency bands (n255 and n256). This has been computed using the Polyfit function of the Python package Numpy [50]. This function implements a polynomial least squares fitting [51]. As input, it takes the ADEV for each SNR scenario simulated, and as output, it provides the minimum SNR required to achieve a certain frequency error (152 Hz for n255 and 198 Hz for n256).

D. NTN LINK BUDGET PARAMETERS

To establish a realistic simulation environment, a complete link budget was computed for a downlink channel from a full gNB regenerative payload in a satellite to a mobile phone in the n255 and n256 frequency bands. The methodology is based on the scenario provided in [52] (3GPP NR-NTN link

TABLE 6. NTN link budget parameters for two NTN frequency bands (n255 and n256). The notation is defined as follows: f_o, carrier frequency; BW, signal bandwidth; h, orbit altitude; EL, minimum satellite elevation angle; d, slant range; L_{tx}, transmission losses; L_{FSPL}, Free-Space Path Loss (FSPL); $L_{channel}$, channel losses (encompassing atmospheric, scintillation, shadowing, and polarization); G_{tx}, satellite antenna gain; P_{tx}, required transmitter power; and SNR, minimum SNR.

Parameter	Value
f_o	2.2 GHz (n256) - 1.55 GHz (n255)
BW	7.2 MHz
h	600 km
EL_{min}	30º
d(at 30º)	1200 km
L_{tx}	3.5 dB
L_{FSPL}	157.83 dB (n255) - 160.87 dB (n256)
$L_{channel}$	8.4 dB
G_{tx}	30 dB
P_{tx} (required)	46.76 dBm (n255) - 49.8 dBm (n256)
Pathloss model	LOS
Minimum SNR	5 dB

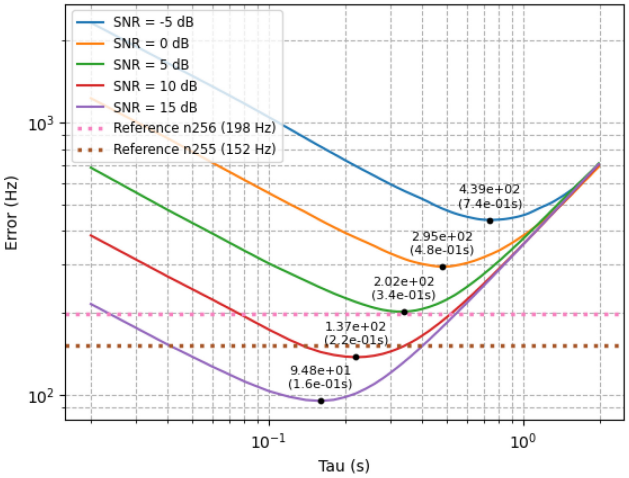

FIGURE 10. Allan Deviation (ADEV) as a function of integration time (τ) for Case No. 1, which uses the reference algorithm, 1 SSB, without the CP.

budget template). The detailed derivation of each parameter is provided in Appendix A, with a summary of the key values listed in Table 6.

The analysis determines that the minimum required SNR for reliable data decoding is 5 dB. This threshold serves as the central point for the simulations in this study, for which an SNR range of –5 dB to 15 dB has been defined.

Based on the complete link budget, the required Effective Isotropic Radiated Power (EIRP) to achieve this minimum SNR is 76.76 dBm (for n255) and 79.8 dBm (for n256). Assuming a satellite transmitter antenna with a gain of 30 dB, as suggested in the 3GPP NR-NTN link budget template [52], the necessary transmitted power is 46.76 dBm (∼50 W) for n255, and 49.80 dBm (∼100 W) for n256. This antenna gain also defines the service coverage, providing a Half-Power Beamwidth (HPBW) of 4°, which results in a footprint of approximately 42 km in diameter [53].

VI. RESULTS

The discussion of the results is divided into two main blocks: first, the frequency error achieved; and second, the minimum SNR required for achieving synchronization.

A. FREQUENCY ERROR

This subsection discusses the results obtained with the baseline case and the impact that each algorithm improvement had on the resulting estimation frequency error.

1) THE BASELINE

It is recalled that the baseline case consists of the reference PSS detection algorithm without the inclusion of the CP in the correlation, and the transmission of a single SSB. This configuration corresponds to case No. 1 in Table 4. The ADEV is presented in Fig. 10, where the vertical axis shows the frequency error and the horizontal axis the integration time. The black dots indicate the minimum error achieved and its respective maximum integration time. It can be observed that there is a decreasing trend in both the frequency error and the integration time when the SNR increases. The performance varies depending on the frequency band implemented, whereas the n256 band almost meets the 3GPP requirement at 0 dB, the n255 band requires approximately 10 dB of SNR to meet the requirement.

For the baseline case, the minimum frequency error and its respective maximum integration time (which is translated into the number of integrated SSBs based on the standard 3GPP periodicity of 20 ms) have been listed in Table 7. This will serve as the basis for discussing the impact of the proposed improvements. Table 7 shows the difference between the obtained error and the 3GPP requirement specifications (152 Hz for n255 and 198 Hz for n256) expressed as a percentage. It can be observed that the performance improves for higher SNR values, as indicated by the negative percentages, which represent a reduction in error. Furthermore, it is relevant to note that the maximum integration time indicates that SS bursts cannot be integrated indefinitely. There are optimal configurations according to the available SNR. The results follow an expected general trend showing that high SNRs reduce the need for long integration periods, which indicates that fewer SSBs are sufficient for achieving accurate frequency estimation.

2) IMPACT OF IMPROVEMENTS

Recall the aspects implemented in the algorithm under test to improve the performance: first, adding the CP in the correlations (combination No. 2); second, integrating 4 SSBs instead of a single SSB (combination No. 3); and third, the enhanced algorithm (combination No. 5). In Fig. 11, the ADEV of the three cases is presented. Moreover, Table 8 shows the improvement in frequency error for each case, expressed as a percentage relative to the baseline. Comparing the three cases, it can be observed that the element that improved the performance the most has been the integration

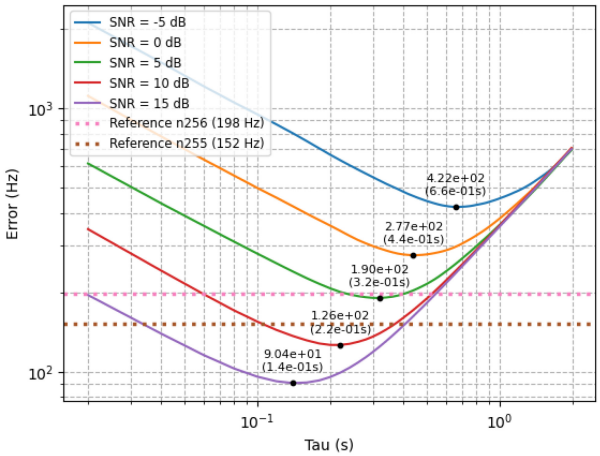

(a) Case No. 2: Reference algorithm, 1 SSB, CP included.

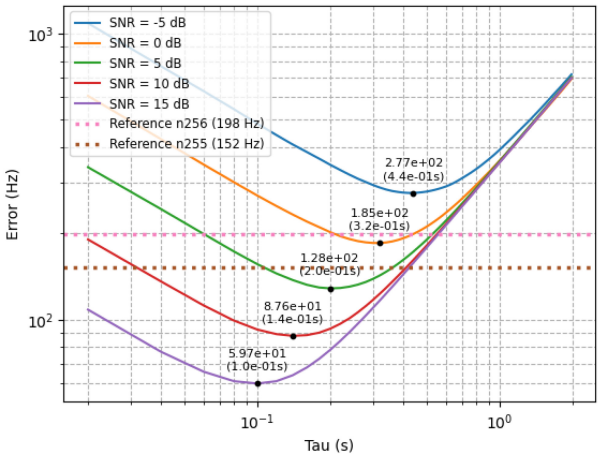

(b) Case No. 3: Reference algorithm, 4 SSBs, without CP.

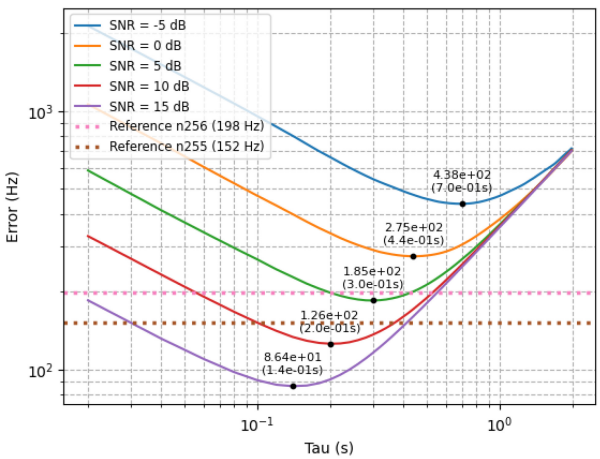

(c) Case No. 5: Enhanced algorithm, 1 SSB, without CP.

FIGURE 11. Performance comparison of the implemented algorithm improvements, showing the Allan Deviation (ADEV) as a function of integration time (τ).

of multiple SSBs. The transmission of four SSBs within the SS burst increased the detection accuracy more than 35% for all SNRs. Furthermore, integration time has also been

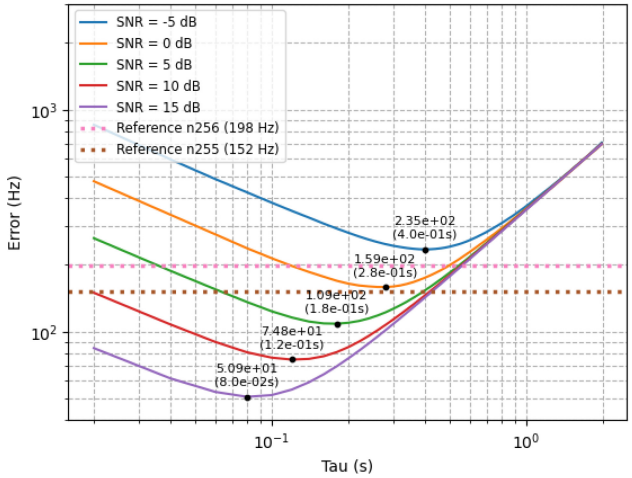

FIGURE 12. Allan Deviation (ADEV) as a function of integration time (τ) for Case No. 8, which uses the enhanced algorithm, four SSBs, and the CP included.

reduced, providing better accuracy for a lower number of integrated SS bursts.

The implementation of the CP and the enhanced algorithm provided slight improvements under 10% in the detection accuracy. However, note that for positioning-critical applications, any improvement in detection is crucial. For that reason, combination No. 8 is also discussed, which applies all enhancements. The improvement of this implementation is indicated as *All applied* in Table 8. The ADEV of this case is presented in Fig. 12. It can be observed that there is a clear improvement in the detection error since both frequency bands met the 3GPP requirement under 0 dB. In particular, the enhancement in the detection accuracy is on average of 44.87% for all SNRs. Depending on the application, any improvement in detection accuracy can be relevant.

3) CRLB COMPARISON

To evaluate the performance of the estimator, the minimum frequency error from the baseline case (Table 7) is compared against its theoretical RMSE_{CRLB}. For this purpose, the analytical RMSE for M integrated SSBs, given in (10), is evaluated based on the single-SSB variance defined in (6). The evaluation parameters are set as follows: N corresponds to the FFT size (256 samples); the sampling period is $T_s = 1/f_s = 130.2$ ns, consistent with Table 3; the Doppler rate is fixed at $\dot{f}_D = 580$ Hz/s; the SS burst periodicity is 20 ms, and the SNR spans the range used in the simulations.

The results of this comparison are detailed in Table 9, and visualized in Fig. 13. The table lists the SNR range, the number of integrated SSBs (M), the resulting RMSE_{CRLB} ($RMSE_M$), and the ratio between the measured error and the theoretical bound.

These RMSE_{CRLB} values illustrate the theoretical lower limit on the frequency estimation error under the impact of a linear frequency drift. Fig. 13 depicts the evolution of both the measured ADEV error and the theoretical RMSE_{CRLB} bound across the evaluated SNR range. A clear

TABLE 7. Performance summary for the baseline case (No. 1), detailing key metrics: minimum frequency error, maximum integration time, number of integrated SSBs, and the frequency error relative to the 3GPP requirement (in %).

SNR	Minimum error	Maximum τ	# SSBs	n255 (152 Hz)	n256 (198 Hz)
-5 dB	439 Hz	0.74 s	37	188.82 %	121.72 %
0 dB	296 Hz	0.48 s	24	94.74 %	49.49 %
5 dB	202 Hz	0.34 s	17	32.89 %	2.02 %
10 dB	138 Hz	0.22 s	11	-9.21 %	-30.30 %
15 dB	95 Hz	0.16 s	8	-37.50 %	-52.02 %

TABLE 8. Performance improvement (%) of several configurations relative to the baseline. The configurations shown are: adding the CP (Case No. 2); using 4 SSBs (Case No. 3); using the enhanced algorithm (Case No. 5); and applying all improvements combined (Case No. 8). Each improvement is evaluated at different SNR levels.

SNR	CP	4 SSB	Enhanced	All applied
- 5 dB	3.87 %	36.90 %	0.23 %	45.56 %
0 dB	6.42 %	37.50 %	7.09 %	44.26 %
5 dB	5.45 %	36.14 %	7.92 %	45.05 %
10 dB	7.97 %	36.23 %	8.70 %	44.20 %
15 dB	4.21 %	36.84 %	8.42 %	45.26 %

TABLE 9. Comparison of the minimum frequency estimation error from the baseline case with the theoretical CRLB for various SNR levels, where: M is the number of integrated SSBs; RMSE_M is the RMSE for M SSBs; and *Ratio* is the proportion between the actual estimation error and the theoretical bound.

SNR	M	RMSE_M	Ratio
-5 dB	37	240 Hz	1.83
0 dB	24	158 Hz	1.87
5 dB	17	111 Hz	1.82
10 dB	11	73 Hz	1.89
15 dB	8	52 Hz	1.83

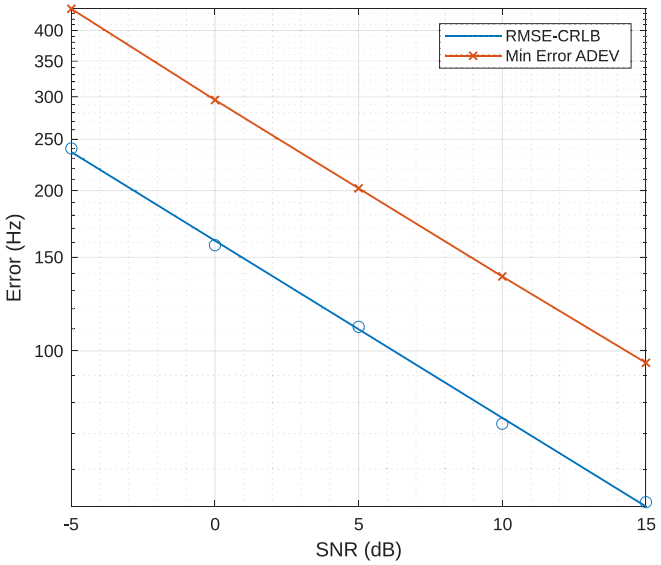

FIGURE 13. Comparison of the ADEV and $\text{RMSE}_{\text{CRLB}}$ (vertical axis) as a function of SNR (horizontal axis).

trend can be observed: higher SNR values correspond to lower error levels. The observed estimator errors do not fall below this theoretical bound. However, a consistent ratio of approximately 1.85 between the simulation error and the RMSE_{CRLB} is observed, indicating room for improving the estimator efficiency. This result is consistent with the literature, as estimation errors in non-ideal scenarios are known to exceed the CRLB by similar factors [54]. While the current theoretical framework incorporates the Doppler rate by assuming a linear frequency drift, the present simulation environment involves complex kinematic behaviors. Specifically, the high Doppler rate characteristic of LEO orbits causes the instantaneous frequency to vary across the duration of the SS bursts. Addressing this phenomenon requires mitigating the time-varying nature of the channel. In literature, complex dynamic effects are typically resolved by implementing joint estimation of coupled parameters [55], [56], [57], [58], as models assuming a constant frequency offset are often insufficient [55], [56]. Consequently, in high-mobility scenarios like NTN, explicitly modeling the Doppler rate becomes essential to accurately characterize the fundamental estimation limits beyond static assumptions. However, extending the proposed model to account for such non-linear dynamics is beyond the scope of the present study, which focuses on PSS detection rather than maximum-likelihood frequency estimation.

B. MINIMUM SNR REQUIRED

The previous discussion focused on the impact that the proposed implementations had on the reference algorithm in terms of estimation frequency error. This section presents the minimum SNR required to achieve proper frequency synchronization for both NTN frequency bands (n255 and n256).

To do so, two integration times have been set: first, $\tau = 20$ ms, representing the case of integrating a single SS burst; and second, $\tau = 200$ ms, representing the case of integrating 10 SS bursts. After an initial evaluation, it was observed that 200 ms was sufficient to test the algorithm, as the maximum Doppler rate is 580 Hz/s, resulting in 116 Hz between each integration. For each combination under study (No. 1, No. 2, No. 3, No. 5, and No. 8), the minimum SNR required according to the frequency band and integration time is listed in Table 10, and visually compared in Fig. 14. The present discussion not only addresses the minimum SNR required of each combination but also the impact of integrating multiple SS bursts (up to 10 SS bursts in the present study) in two different NTN frequency bands.

TABLE 10. Minimum required SNR for different simulation cases and NTN frequency bands (n255 and n256), evaluated at integration times of 20 ms (1 SSB) and 200 ms (10 SSBs).

No.	No. 1		No. 2		No. 3		No. 5		No. 8	
Freq. band	n255	n256	n255	n256	n255	n256	n255	n256	n255	n256
$\tau = 20$ ms	15.3 dB	14.4 dB	15.0 dB	14.0 dB	10.6 dB	10.6 dB	14.7 dB	13.7 dB	8.6 dB	8.6 dB
$\tau = 200$ ms	10.2 dB	7.6 dB	9.5 dB	6.6 dB	3.6 dB	-0.7 dB	9.2 dB	6.1 dB	0.3 dB	-3.9 dB

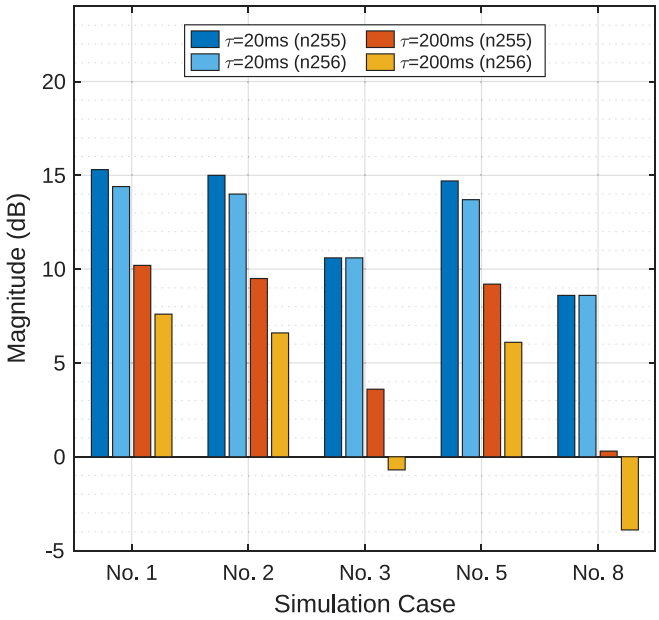

FIGURE 14. Minimum required SNR for NTN bands n255 and n256 at integration times of 20 ms (1 SSB) and 200 ms (10 SSBs). Simulation cases: (No. 1) Baseline; (No. 2) Reference, 1 SSB w/ CP; (No. 3) 4 SSB w/o CP; (No. 5) Enhanced, 1 SSB w/o CP; and (No. 8) Full implementation.

When observing the baseline case (indicated as No. 1 in Fig. 14), the results indicate a significant reduction in the minimum SNR required between integrating a single SS burst (20 ms) and 10 SS bursts (200 ms). For the n255 band, the reduction is of 5 dB, whereas for the n256 band, the SNR is reduced by almost 7 dB. Note that the n255 band requires more SNR to achieve synchronization, as the 0.1 ppm requirement is defined according to the most restrictive frequency of the band.

This SNR reduction is also significant across the remaining combinations (as visibly demonstrated in Fig. 14, with cases) No. 3 and No. 8 showing the greatest reduction. This is consistent with the improvement in detection accuracy that integrating 4 SSBs (No. 3) provides, whereas in n255, the minimum SNR required is reduced by 7 dB, and for n256 it is reduced by more than 10 dB. Furthermore, the lowest SNR required was achieved when applying the complete solution (i.e., all enhancements) and integrating during 200 ms; notably, Fig. 14 highlights this specific scenario (No. 8, n256) as the absolute minimum, reaching negative dB values. Compared to the baseline case, the achieved SNR gain is 15 dB for n255 and 18.3 dB for n256. This improvement is particularly relevant in the NTN context, where the link budget is highly constrained.

Furthermore, the transmission of different SSB within an SS burst is designed to be performed from independent beams. However, the transmission of multiple SSBs and SS bursts from a single beam could offer a significant SNR gain and improve synchronization in GNSS-denied environments. Based on this analysis, the number of SS bursts integrated significantly impacts the accuracy, particularly by increasing it. From the results, it can be concluded that the aspects that most influence detection accuracy are the number of SSBs within the SS burst and the number of SS bursts integrated.

VII. DISCUSSION

A. EXTENDED CP

As it has been shown in Section VI-A.2, the utilization of the CP in the correlations enhanced the accuracy of frequency detection. However, the results did not show a huge improvement. For this reason, the use of the extended CP has been explored by evaluating the accuracy achieved with it. Note that this implementation modifies the slot structure by assigning 12 OFDM symbols to the slot instead of the 14 OFDM symbols for normal CP (as presented in Fig. 8).

In the 3GPP, the extended CP is only available for $\mu = 2$ (a SCS of 60 kHz), as the symbol duration is assumed to be short enough to benefit from the longer CP duration. For other numerologies, it is expected to be inefficient. For the numerology considered in this study ($\mu = 1$), the CP is assumed to be too long compared to the symbol duration, causing an increased CP overhead. Hence, a waste of time. However, in the context of synchronization, the previous results have demonstrated that extended sequences provided increased detection accuracy.

In terms of analyzing the impact of the extended CP, combination No. 2 (reference algorithm with 1 SSB and with CP) has been considered for comparison with the extended CP implementation. The 3GPP defines the duration of the extended CP and provides the CP length in samples [19]. It is necessary to adapt the CP length to the current application using $\mu = 1$ instead of $\mu = 2$. To do so, based on the equations detailed in 3GPP TS 38.211 [19], the CP extended length in samples has been computed using (11). Note that an FFT size of 1024 samples is often assigned to $\mu = 1$ [59]. In the current study, the simulated FFT size is 256 samples, leading to a scaling factor of $\frac{256}{1024}$. The resulting extended CP has a length of 64 samples. Moreover, when implementing

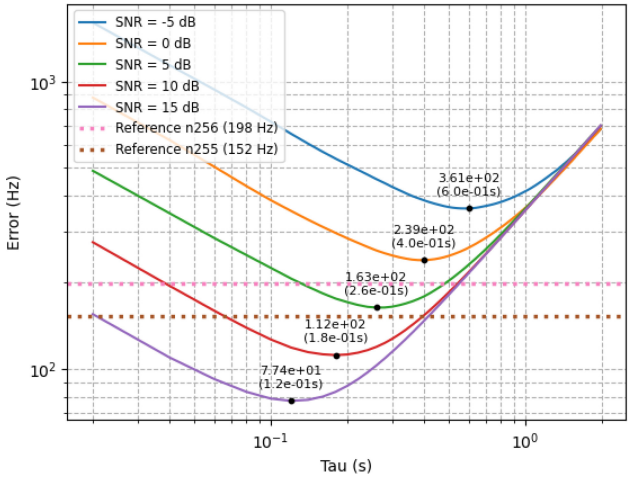

FIGURE 15. Allan Deviation (ADEV) as a function of integration time (τ) for the reference algorithm, one SSB, and the extended CP.

TABLE 11. Minimum required SNR for the baseline and extended CP case, evaluated across two NTN frequency bands (n255 and n256) and two integration times (20 ms for 1 SSB; 200 ms for 10 SSBs).

Freq. band	n255	n256
τ =20 ms	7.6 dB	4.1 dB
τ = 200 ms	14.1 dB	12.9 dB

extended CP, all symbols have the same length, unlike the normal case where the first symbol has a slightly larger length.

$$\begin{cases} N_{CP}^{\mu=1} = 512k \cdot 2^{-\mu} = 512 \cdot 2^{-1} = 256 \text{ samples} \\ N_{CP_{scaled}}^{\mu=1} = 256 \cdot \frac{256}{1024} = 64 \text{ samples} \end{cases} \quad (11)$$

Fig. 15 shows the resulting ADEV for combination No. 2. The detection accuracy improved when compared to the normal CP case (Fig. 11(a)), and the integration time was also reduced. Furthermore, when comparing the results to those obtained with the baseline, on average, whereas the normal CP provided an improvement of around 6%, the extended CP gives an improvement on average of 18.4%. In terms of the minimum SNR required (listed in Table 11), the extended CP compared to the baseline provides a 3 dB SNR gain, and 2 dB when compared to combination No. 2. Overall, despite the higher overhead associated with $\mu = 1$, the extended CP has proven to yield significantly greater improvements than the normal CP, particularly in terms of detection accuracy and SNR performance.

B. PRACTICAL CONSIDERATIONS

The practical deployment of a synchronization algorithm, particularly in NTN scenarios, requires considering system-level and device-level constraints. As discussed earlier, the transmission of multiple SS bursts is designed to be performed from multiple gNBs. In this study, the transmission from a single beam is proposed. This directly impacts the requirements of the physical characteristics of the antennas. High directivity antennas are essential for ensuring a sufficient link budget, considering the rapid motion and long distances that characterize LEO scenarios. To improve signal detection, antennas must be equipped with high gain and narrow beams.

However, a key trade-off exists between antenna directivity and coverage area. As shown in the results, lower SNR required (as enabled by the proposed algorithm) allows the use of antennas with lower directivity, which in turn increases the coverage area. As listed in Table 6, a transmitter antenna gain of 30 dB initially provided a coverage of 42 km. Conversely, reducing the gain by 15 dB expands the coverage to 240 km [53]. Such an improvement allows a single gNB to serve broader areas, reducing the need for handovers while maintaining synchronization reliability. This is particularly beneficial in remote areas, where hardware availability is limited. In addition, the implementation allows using small and cost-effective platforms, which is crucial to deploy massive constellations. However, note that whereas a lower-gain antenna may expand the area where a UE can successfully detect the PSS and synchronize, the SNR at the cell edge might be insufficient to support high-throughput services. According to Block Error Rate (BLER)-SNR results for NR Modulation and Coding Scheme (MCS) under AWGN conditions [60], low-order modulations such as Quadrature Phase Shift Keying (QPSK) (and BPSK as the PSS) with a low coding rate can achieve an acceptable BLER ($\sim 10^{-2}$) at SNR levels around 0-5 dB. In contrast, higher-order modulations require higher SNRs to reach comparable error rates. Therefore, at the cell edge, where the SNR typically remains low, only low MCS schemes can be reliably supported, limiting the achievable throughput.

Moreover, the computational complexity of the algorithm directly influences its real-world viability. Advanced synchronization algorithms often impose a significant processing burden on the UE, which translates into two critical limitations: device cost and power consumption. This may potentially hinder the adoption in cost-sensitive markets like Internet of Things (IoT) [61]. Particularly, the initial cell search is one of the most energy-intensive procedures for a UE [62]. The solution presented in this work addresses this challenge by introducing configurable transmission schemes with a critically low computational overhead compared to the reference algorithm. Conversely, for scenarios where maximum accuracy is paramount, and resources permit, an enhanced algorithm that delivers superior performance at the cost of a moderate increase in complexity is also proposed.

Specifically, the impact of the proposed enhancements varies significantly. The inclusion of the CP (Case No. 2) results in a marginal computational increase ($\approx$ 10%) compared to the baseline (Case No. 1) due to the larger number of processed samples. In contrast, the enhanced algorithm (Case No. 8) demands significantly higher processing power, as the refined search stage requires executing a denser grid of FFTs for precise estimation. While Case No. 8 delivers the highest sensitivity gains (up to 18.3 dB for n256), making it the optimal choice for performance-critical research contexts,

it represents the most computationally expensive option for practical deployment.

Beyond computational processing, the specific implementation implications of integrating multiple SS bursts must be addressed. The integration of multiple SS bursts (e.g., comparing Case No. 3 with 4 SSBs against the baseline Case No. 1) inherently expands the required acquisition window, which directly impacts the time to obtain a reliable fix or successfully execute the initial access procedure [63]. This leads to a deterministic increase in latency, which is particularly critical for energy-constrained IoT devices where prolonged active reception states deplete battery life [33].

Concurrent with latency, the memory requirements represent a critical design constraint. However, distinct from the latency penalty, the impact on memory buffering is notably mitigated by the non-coherent integration scheme employed. Instead of storing the raw I/Q samples for the entire duration of all bursts simultaneously, the receiver accumulates intermediate correlation results iteratively. Consequently, the additional memory footprint required for buffering multiple bursts is negligible. This efficiency is crucial given that NTN devices already operate under stringent hardware constraints due to the processing of long Round Trip Time (RTT) links [64].

VIII. CONCLUSION

The present contribution proposes and evaluates an enhanced frequency estimation technique based on the 5G-NR PSS for NTN scenarios. The analysis assessed the impact of several key elements on detection accuracy: the use of the CP in signal correlations, the transmission of four SSBs per SS burst, an enhanced algorithm with a refined search, and the integration of multiple SS bursts. The evaluation was conducted via Monte Carlo simulations across a range of SNR values in two NTN frequency bands, n255 (L-band) and n256 (S-band).

The results demonstrate the feasibility of achieving initial synchronization without relying on GNSS. Although GNSS signals typically enable superior frequency accuracy (e.g., in the parts per billion (ppb) range [65]), the proposed method proves sufficient to successfully meet the 3GPP requirement of 0.1 ppm, frequency accuracy under NTN constraints. This was particularly evident when multiple SSBs and SS bursts were integrated, which were identified as the elements having the most significant impact on performance. Furthermore, the incorporation of the CP and the enhanced detection algorithm further contributed to improving frequency accuracy, reinforcing the benefits of leveraging longer signal sequences and advanced processing techniques.

Particularly, the proposed enhancements reduced the error by up to 36.72% when using 4 SSBs, and by 44.87% when combining all improvements, achieving SNR gains of 7 dB (10 dB) for n255 (n256) with partial solutions and up to 15 dB (18.3 dB) with the complete solution. The proposed implementation enables a reduction in the minimum SNR required, highlighting its viability when using antennas with lower directivity and broader coverage. This leads to a less demanding antenna. This work demonstrates the potential for achieving GNSS-free PNT in 5G/6G systems, where maintaining a highly accurate synchronized carrier is key to achieving low positioning errors, thereby addressing the critical need for global and resilient connectivity.

APPENDIX A
NTN LINK BUDGET DEFINITION

The definition of a single, universally adopted standard for NTN link budgets is still under development. Therefore, the methodology for the present study is based on the 3GPP NR-NTN link budget template provided in [52]. This template details the scenario, geometry, and path loss models. Its parameters have been complemented with specific values extracted from 3GPP technical specifications [17], [18] and academic literature to ensure a realistic model.

The link budget is designed to satisfy a minimum SNR (SNR_{min}) at the receiver. In 3GPP TS 38.101 [18], a reference SNR of 9 dB is specified for QPSK modulation. Considering a coding rate of 0.3 for robust communication, the effective minimum required SNR is 3.77 dB. To incorporate design margin, this value is rounded up to $SNR_{min} = 5$ dB. As the present study targets PNT applications with synchronization requirements, the navigation message needs to be successfully decoded; merely detecting the signal may not be sufficient. This justifies this conservative approach.

The total noise power (P_N) at the receiver is calculated by integrating the thermal noise density over the signal bandwidth (BW) and adding the noise generated internally by the receiver, which is quantified by its Noise Figure (NF). The expression for the noise power in dBm is given in (12). N_0 corresponds to the thermal noise power density, with a standard value of –174 dBm/Hz at room temperature (T = 290 K). BW is the receiver bandwidth, which is set to match the signal bandwidth. For the SSB, this corresponds to its 240 subcarriers with an SCS of 30 kHz, resulting in BW = 7.2 MHz. The NF is derived from the N_{oc} value for a power class 1 UE (3GPP TS 38.101-4 [18]), resulting in NF = 6.7 dB.

$$P_N\ (\text{dBm}) = N_0 + 10\log_{10}(\text{BW}) + \text{NF} \tag{12}$$

With the required SNR_{min} and the calculated P_N, the minimum receiver power ($P_{rx,min}$) can be determined as in (13).

$$P_{rx,min}(\text{dBm}) = SNR_{min} + P_N \tag{13}$$

The signal power transmitted from the gNB is attenuated by a series of losses before reaching the receiver. The first loss is the FSPL (L_{FSPL}), which depends on frequency and distance. It has been calculated for two carrier frequencies fo_{n255}= 1.55 GHz and fo_{n256}= 2.2 GHz. The geometry is based on the 3GPP template [52], assuming a LEO satellite at a 600 km altitude h) and a minimum elevation angle of $\text{EL}_{min} = 30°$. This results in a slant range of d =1200 km

and an L_{FSPL} of 157.83 dB (n255) and 160.87 dB (n256). The second channel losses ($L_{channel}$) encompass atmospheric, scintillation, shadowing, and polarization losses. Following the 3GPP template [52] for a Line-of-Sight (LoS) scenario, these are collectively estimated at $L_{channel} = 8.4$ dB. The third and final loss is due to transmission losses (L_{tx}), which are estimated at 3.5 dB, based on [66]. This value includes a 3 dB margin to account for potential beam misalignment.

To determine the required transmitter power (P_{tx}), the Friis equation (14) has been used. This expression includes the required EIRP from the satellite, which determines P_{tx}, given (15). The EIRP involves P_{tx} and the satellite antenna gain (G_{tx}). A typical gain for the mobile phone antenna of $G_{rx} = 0$ dBi has been assumed [67].

$$P_{rx}(dBm) = \text{EIRP} + G_{rx} - L_{tx} - L_{FSPL} - L_{channel} \quad (14)$$

$$\text{EIRP} = G_{tx} + P_{tx} \quad (15)$$

The final results of these calculations for both frequency bands are presented in Table 6 in the main body of the paper.

APPENDIX B
DERIVATION OF THE CRAMER RAO LOWER BOUND

The general expression for the CRLB is defined as in (16) (from [45]), where $var(\hat{\Delta f})$ corresponds to the variance of the estimator, Δf is the frequency offset to be estimated, and $I(\Delta f)$ is the Fisher information function [68]. For this derivation, the Fisher information is defined as the expected value of the squared score function (the first derivative of the log-likelihood function) [45], as presented in (17) (from [45]), where $p(x; \Delta f)$ represents the likelihood function and x the collection of received samples.

$$var\left(\hat{\Delta f}\right) \geq \frac{1}{I(\Delta f)} \quad (16)$$

$$I(\Delta f) = \mathbb{E}\left[\left(\frac{\partial}{\partial \Delta f} \ln p(x, \Delta f)\right)^2\right] \quad (17)$$

The starting point of the computation is the model of the received signal in the discrete-time domain. The received signal containing the PSS can be modeled as presented in (18) [45], [69], where $s[n]$ is the known time-domain PSS sequence, Δf is the frequency offset to be estimated, T_s is the sampling period, and $w[n]$ is complex AWGN with variance σ^2.

$$x[n] = s[n] \cdot e^{j2\pi \Delta f n T_s} + w[n] \quad (18)$$

The foundation of the Fisher information function is the likelihood function, which describes the probability of observing the complete data set x for a given value of Δf [45], [70]. Since the noise is Gaussian and white, the joint likelihood function can be defined as the product of individual Probability Density Function (PDF)s [45] as presented in (19).

$$p(x; \Delta f) = \prod_{n=0}^{N-1} \frac{1}{\pi \sigma^2} \exp\left(-\frac{|x[n] - s[n]e^{j2\pi \Delta f n T_s}|^2}{\sigma^2}\right) \quad (19)$$

To simplify the mathematical analysis, the log-likelihood function is computed by applying the logarithm operator, transforming the product PDFs into a sum [45]. The log-likelihood, denoted as $\ln p(x; \Delta f)$, is defined as in (20).

$$\ln p(x; \Delta f) = -N \ln\left(\pi \sigma^2\right) - \frac{1}{\sigma^2} \sum_{n=0}^{N-1} \left|x[n] - s[n]e^{j2\pi \Delta f n T_s}\right|^2 \quad (20)$$

Subsequently, the term $\frac{\partial}{\partial \Delta f} \ln(x, \Delta f)$ in (17) corresponds to the score function [45], which corresponds to the first derivative of the log-likelihood function with respect to the parameter Δf. The result of this derivation is shown in (21).

$$\frac{\partial}{\partial \Delta f} \ln f(x; \Delta f) = \frac{2}{\sigma^2} \Re\left\{\sum_{n=0}^{N-1} \left(x[n] - s[n]e^{j2\pi \Delta f n T_s}\right) \cdot \left(s[n] \cdot j2\pi n T_s \cdot e^{j2\pi \Delta f n T_s}\right)^*\right\} \quad (21)$$

The next step involves the computation of the expected value of the squared score function. The signal model from (18) is substituted into the score function (21). This step is fundamental, as the deterministic signal component cancels out, leaving an expression for the score that is a function of only the random noise samples $w[n]$. The computation of $E[\cdot]$ relies on the statistical properties of the AWGN. Specifically, the noise samples $w[n]$ are modeled as zero-mean and statistically independent complex random variables [45], [70]. This implies the following properties (22), (23), and (24):

$$\text{E}[w[n]] = 0, \qquad \forall n \quad (22)$$

$$\text{E}\left[w[n]^* w[m]\right] = 0, \qquad n \neq m \quad (23)$$

$$\text{E}\left[|w[n]|^2\right] = \sigma^2 \quad (24)$$

When squaring the summation in the simplified score function, a double summation over indices n and m arises. Due to the independence property of the noise, all cross-terms where $n \neq m$ have an expected value of zero and thus vanish from the expression [45]. Consequently, the calculation simplifies considerably, leaving only the diagonal terms where $n = m$. Evaluating the expectation of these remaining terms, and utilizing the variance property, yields the final expression for the Fisher information (25).

$$I(\Delta f) = \frac{2}{\sigma^2} \sum_{n=0}^{N-1} |s[n]|^2 (2\pi n T_s)^2 \quad (25)$$

To obtain the final CRLB expression, the PSS sequence is assumed to have a constant amplitude, such that $|s[n]|^2 = A^2$, and defining the linear SNR expression as $SNR = \frac{A^2}{\sigma^2}$. The summation term is a standard sum of integer powers [71], which can be expressed by (26), where N denotes the total number of samples.

$$\sum_{n=0}^{N-1} n^2 = \frac{N(N-1)(2N-1)}{6} \quad (26)$$

By substituting these elements into (16) and inverting the Fisher information from (25), the CRLB expression of the proposed frequency estimator is obtained, as presented in Section V-B.2 (6).

REFERENCES

[1] M. Brambilla et al., "Integration of 5G and GNSS technologies for enhanced positioning: An experimental study," *IEEE Open J. Commun. Soc.*, vol. 5, pp. 7197–7215, 2024.

[2] W. Stock, R. T. Schwarz, C. A. Hofmann, and A. Knopp, "Survey on opportunistic PNT with signals from LEO communication satellites," *IEEE Commun. Surveys Tut.*, vol. 27, no. 1, pp. 77–107, Feb. 2025.

[3] "Technical specification group radio access network; study on expanded and improved NR positioning; (Release 18)," 3GPP, Sophia Antipolis, France, Rep. TR 38.859, 2024. [Online]. Available: https://www.3gpp.org/

[4] W. Jiang, B. Han, M. A. Habibi, and H. D. Schotten, "The road towards 6G: A comprehensive survey," *IEEE Open J. Commun. Soc.*, vol. 2, pp. 334–366, 2021.

[5] C. T. Nguyen et al., "Emerging technologies for 6G non-terrestrial-networks: From academia to industrial applications," *IEEE Open J. Commun. Soc.*, vol. 5, pp. 3852–3885, 2024.

[6] A. Gonzalez-Garrido, J. Querol, and S. Chatzinotas, "5G positioning reference signal configuration for integrated terrestrial/non-terrestrial network scenario," in *Proc. IEEE/ION Position, Locat. Navig. Symp. (PLANS)*, 2023, pp. 1136–1142.

[7] W.-Y. Yeo and D.-J. Lee, "Uplink time synchronization based on time drift measurements in non-terrestrial networks," *IEEE Access*, vol. 12, pp. 168877–168893, 2024.

[8] A. K. Meshram, S. Kumar, J. Querol, S. Andrenacci, and S. Chatzinotas, "Reduced complexity initial synchronization for 5G NR multibeam LEO-based non-terrestrial networks," *IEEE Open J. Commun. Soc.*, vol. 6, pp. 1528–1551, 2025.

[9] R. Tuninato and R. Garello, "5G ntn primary synchronization signal: An improved detector for handheld devices," *IEEE Open J. Commun. Soc.*, vol. 5, pp. 3792–3803, 2024.

[10] *Physical Layer Procedures for Control, Release 17*, 3GPP Standard TS 38.213, 2022. [Online]. Available: https://www.3gpp.org/

[11] X. Lin, Z. Lin, S. E. Löwenmark, J. Rune, and R. Karlsson, "Doppler shift estimation in 5G new radio non-terrestrial networks," in *Proc. IEEE Glob. Commun. Conf. (GLOBECOM)*, 2021, pp. 1–6.

[12] M. Abuyaghi, S. Si-Mohammed, G. Shaker, and C. Rosenberg, "Positioning in 5G networks: Emerging techniques, use cases, and challenges," *IEEE Internet Things J.*, vol. 12, no. 2, pp. 1408–1427, Jan. 2025.

[13] Y. Liao, S. Liu, X. Hong, J. Shi, and L. Cheng, "Integration of communication and navigation technologies toward LEO-enabled 6G networks: A survey," *Space, Sci. Technol.*, vol. 3, p. 92, Oct. 2023.

[14] Y.-H. You and H.-K. Song, "Efficient sequential detection of carrier frequency offset and primary synchronization signal for 5G NR systems," *IEEE Trans. Veh. Technol.*, vol. 69, no. 8, pp. 9212–9216, Aug. 2020.

[15] B. W. Stevens and M. F. Younis, "Detection algorithm for cellular synchronization signals in airborne applications," *IEEE Access*, vol. 9, pp. 55555–55566, 2021.

[16] S. Yan and Y. Tian, "A novel fast synchronization strategy for primary synchronization signal in 5G new radio systems," in *Proc. 3rd Int. Conf. Comput., Commun., Percept. Quantum Technol. (CCPQT) 2024*, 2024, pp. 123–126.

[17] *Base Station (BS) Radio Transmission and Reception, Release 17*, 3GPP Standard TS 138.104, 2022. [Online]. Available: https://www.3gpp.org/

[18] *User Equipment (UE) Radio Transmission and Reception; Part 1: Range 1 Standalone, Release 17*, 3GPP Standard TS 38.101, 2023. [Online]. Available: https://www.3gpp.org/

[19] *Physical Channels and Modulation, Release 16*, 3GPP Standard TS 38.211, 2020. [Online]. Available: https://www.3gpp.org/

[20] M. R. Sriharsha, S. Dama, and K. Kuchi, "A complete cell search and synchronization in LTE," *Eurasip J. Wireless Commun. Netw.*, vol. 101, pp. 1–14, May 2017.

[21] R. Tuninato, D. G. Riviello, R. Garello, B. Melis, and R. Fantini, "A comprehensive study on the synchronization procedure in 5G NR with 3GPP-compliant link-level simulator," *EURASIP J. Wireless Commun. Netw.*, vol. 2023, p. 111, Oct. 2023.

[22] M. Morelli and M. Moretti, "A robust maximum likelihood scheme for PSS detection and integer frequency offset recovery in LTE systems," *IEEE Trans. Wireless Commun.*, vol. 15, no. 2, pp. 1353–1363, Feb. 2016.

[23] Y.-H. You, Y.-A. Jung, S.-C. Choi, and I. Hwang, "Complexity-effective sequential detection of synchronization signal for cellular narrowband IoT communication systems," *IEEE Internet Things J.*, vol. 8, no. 4, pp. 2900–2909, Feb. 2021.

[24] J. J. Van De Beek, M. Sandell, and P. O. Borjesson, "ML estimation of time and frequency offset in OFDM systems," *IEEE Trans. Signal Process.*, vol. 45, no. 7, pp. 1800–1805, Jul. 1997.

[25] S. Yoneda, M. Sawahashi, and S. Nagata, "Physical cell ID detection probability in the presence of CFO including doppler shift for NR TN and NTN," in *Proc. VTS Asia Pac. Wireless Commun. Symp. (APWCS)*, 2023, pp. 1–5.

[26] *Service Requirements for the 5G System, Version 15.9.0, Release 15*, 3GPP Standard TS 122.261, 2021. [Online]. Available: https://www.3gpp.org/

[27] L. Italiano, B. C. Tedeschini, M. Brambilla, H. Huang, M. Nicoli, and H. Wymeersch, "A tutorial on 5G positioning," *IEEE Commun. Surveys Tut.*, vol. 27, no. 3, pp. 1488–1535, Jun. 2025.

[28] S. Huang, H.-M. Chen, B. Wang, J. Chai, X. Wu, and F. Li, "Positioning performance evaluation for 5G positioning reference signal," in *Proc. 2nd Int. Conf. Front. Electron., Inf. Comput. Technol. (ICFEICT)*, 2022, pp. 497–504.

[29] A. A. Zaidi, R. Baldemair, V. Moles-Cases, N. He, K. Werner, and A. Cedergren, "OFDM numerology design for 5G new radio to support IoT, eMBB, and MBSFN," *IEEE Commun. Stand. Mag.*, vol. 2, no. 2, pp. 78–83, Jun. 2018.

[30] S. Huang, Y. Su, Y. He, and S. Tang, "Joint time and frequency offset estimation in LTE downlink," in *Proc. 7th Int. Conf. Commun. Netw. China*, 2012, pp. 394–398.

[31] C. Yang, M. Miller, E. Blasch, and T. Nguyen, "Comparative study of coherent, non-coherent, and semi-coherent integration schemes for GNSS receivers," in *Proc. 63rd Annu. Meeting Inst. Navig.*, 2007, pp. 572–588.

[32] R. Khan, S. U. Khan, R. Zaheer, and S. Khan, "Acquisition strategies of GNSS receiver," in *Proc. Int. Conf. Comput. Netw. Inf. Technol. (ICCNIT)*, 2011, pp. 119–124.

[33] Q. Qi, T. Hong, and G. Zhang, "Positioning-based uplink synchronization method for NB-IoT in LEO satellite networks," *Symmetry*, vol. 17, no. 7, p. 984, 2025.

[34] K. Shamaei, J. Khalife, and Z. M. Kassas, "Exploiting LTE signals for navigation: Theory to implementation," *IEEE Trans. Wireless Commun.*, vol. 17, no. 4, pp. 2173–2189, Apr. 2018.

[35] Y.-H. You, J.-H. Park, and I.-Y. Ahn, "Complexity effective sequential detection of secondary synchronization signal for 5G new radio communication systems," *IEEE Syst. J.*, vol. 15, no. 3, pp. 3382–3390, Sep. 2021.

[36] T. Bhatt, "Sequences with perfect periodic auto and cross correlation properties," *Traitement du Signal*, 37, pp. 477–484, Jun. 2020.

[37] S. Winograd, *Arithmetic Complexity of Computations* (CBMS-NSF Regional Conference Series in Applied Mathematics). Philadelphia, PA, USA: Soc. Ind. Appl. Math., 1980.

[38] B. Barth et al., "The 5G-non-terrestrial network channel in a railway environment: Characteristics and required subcarrier spacing," *IEEE Veh. Technol. Mag.*, vol. 20, no. 3, pp. 78–86, Sep. 2025.

[39] B.-H. Yeh, J.-M. Wu, and R. Y. Chang, "Efficient doppler compensation for LEO satellite downlink OFDMa systems," *IEEE Trans. Veh. Technol.*, vol. 73, no. 12, pp. 18863–18877, Dec. 2024.

[40] S. Yoneda, M. Sawahashi, and S. Nagata, "Comparisons of physical cell id detection methods with carrier frequency offset compensation for millimeter-wave bands," in *Proc. IEEE 96th Veh. Technol. Conf. (VTC)*, 2022, pp. 1–6.

[41] A. Zaidi, F. Athley, J. Medbo, U. Gustavsson, G. Durisi, and X. Chen, "Chapter 5—Multicarrier waveforms," in *5G Physical Layer*, A. Zaidi, F. Athley, J. Medbo, U. Gustavsson, G. Durisi, and X. Chen, Eds., Cambridge, MA, USA: Academic, 2018, pp. 119–158.

[42] Q. Bader, H. Salem, H. Elghamrawy, and A. Noureldin, "Doppler-based positioning with LEO satellites: A survey of techniques, challenges, and opportunities," TechRxiv, Preprint, 2025. [Online]. Available: http://dx.doi.org/10.36227/techrxiv.175001088.84355523/v1
[43] (Iowa State Univ., Ames, IA, USA). *Allan Variance*. Accessed: May 22, 2025. [Online]. Available: https://home.engineering.iastate.edu/shermanp/AERE432/lectures/Rate n.d
[44] E. Dai, L. Su, and Y. Ge, "Cramer–Rao lower bound for frequency estimation of sinusoidal signals," *IEEE Trans. Instrum. Meas.*, vol. 73, pp. 1–7, 2024.
[45] S. M. Kay, "Cramér-rao lower bound," in *Fundamentals of Statistical Signal Processing, Volume I: Estimation Theory*. Englewood Cliffs, NJ, USA: Prentice Hall, 1993, pp. 27–52.
[46] W. J. Riley, *Handbook of Frequency Stability Analysis*. Nat. Inst. Stand. Technol., Gaithersburg, MD, USA, 2018.
[47] I. Leyva-Mayorga, F. Saggese, L. Li, and P. Popovski, "Integrating atmospheric sensing and communications for resource allocation in NTNs," *IEEE Trans. Wireless Commun.*, vol. 24, no. 11, pp. 9703–9718, Nov. 2025.
[48] D. Wang, Z. Mei, H. Zhang, and H. Li, "A novel PSS timing synchronization algorithm for cell search in 5G NR system," *IEEE Access*, vol. 9, pp. 5870–5880, 2021.
[49] "Python package index (PyPI)." Allantools. 2024. [Online]. Available: https://pypi.org/project/AllanTools/
[50] "NumPy developers copyright." Numpy.polyfit. 2008–2024. [Online]. Available: https://numpy.org/doc/stable/reference/generated/numpy.polyfit.html
[51] S.A. Dyer and X. He, "Least-squares fitting of data by polynomials," *IEEE Instrum. Meas. Mag.*, vol. 4, no. 4, pp. 46–51, Dec. 2001.
[52] "Link budget template NTN," 3GPP, Gothenberg, Sweden, document TSG RAN WG1 meeting #103e, 2020. [Online]. Available: https://www.3gpp.org/
[53] K. P. Spies, "Calculation of geostationary satellite footprints for certain applications," Fed. Commun. Comm., Washington, DC, USA, Rep. 80-51, 1980.
[54] Z. Wei et al., "5G PRS-based sensing: A sensing reference signal approach for joint sensing and communication system," *IEEE Trans. Veh. Technol.*, vol. 72, no. 3, pp. 3250–3263, Mar. 2023.
[55] M. Morelli and U. Mengali, "Carrier-frequency estimation for transmissions over selective channels," *IEEE Trans. Commun.*, vol. 48, no. 9, pp. 1580–1589, Sep. 2000.
[56] A. Barbieri and G. Colavolpe,"On the Cramer-Rao bound for carrier frequency estimation in the presence of phase noise," *IEEE Trans. Wireless Commun.*, vol. 6, no. 2, pp. 575–582, Feb. 2007.
[57] C. Shengyao and X. Feng, "Cramer-Rao bounds for the joint delay-doppler estimation of compressive sampling pulse-doppler radar," *J. Syst. Eng. Electron.*, vol. 29, no. 1, pp. 58–66, Feb. 2018.
[58] T. Zhao and T. Huang, "Cramer-Rao lower bounds for the joint delay-doppler estimation of an extended target," *IEEE Trans. Signal Process.*, vol. 64, no. 6, pp. 1562–1573, Mar. 2016.
[59] *Base Station (BS) Conformance Testing Part 1: Conducted Conformance Testing, Release 15*, 3GPP Standard TS 38.141-1, 2019. [Online]. Available: https://www.3gpp.org/
[60] L. Méndez-Monsanto, A. MacQuarrie, M. R. Ghourtani, M. J. L. Morales, A. G. Armada, and A. Burr, "BLER-SNR curves for 5G NR MCS under AWGN channel with optimum quantization," In *Proc. IEEE 100th Veh. Technol. Conf. (VTC)*, 2024, pp. 1–6.
[61] F. Tong, Y. Sun, and S. He, "On positioning performance for the narrow-band Internet of Things: How participating eNBs impact?" *IEEE Trans. Ind. Informat.*, vol. 15, no. 1, pp. 423–433, Jan. 2019.
[62] W. B. Abbas and M. Zorzi, "Context information based initial cell search for millimeter wave 5G cellular networks," in *Proc. Eur. Conf. Netw. Commun. (EuCNC)*, 2016, pp. 111–116.
[63] V. R. Chandrika, J. Chen, L. Lampe, G. Vos, and S. Dost, "SPIN: Synchronization signal-based positioning algorithm for IoT nonterrestrial networks," *IEEE Internet Things J.*, vol. 10, no. 23, pp. 20846–20867, Dec. 2023.
[64] "Technical specification group radio access network; study on new radio (NR) to support non-terrestrial networks; (Release 15)," 3GPP, Sophia Antipolis, France, Rep. TR 38.811, 2019. [Online]. Available: https://www.3gpp.org/
[65] E. Kaplan and C. Hegarty, *Understanding GPS/GNSS: Principles and Applications*. 3rd ed. Norwood, MA, USA: Artech House, 2017.
[66] D. Rozenvasser and K. Shulakova, "Estimation of the starlink global satellite system capacity," in *Proc. 11th ICAIIT*, 2024, pp. 55–60.
[67] Z. Xu, Y. Gao, G. Chen, R. Fernandez, V. Basavarajappa, and R. Tafazolli, "Enhancement of satellite-to-phone link budget: An approach using distributed beamforming," *IEEE Veh. Technol. Mag.*, vol. 18, no. 4, pp. 85–93, Dec. 2023.
[68] A. Ly, M. Marsman, J. Verhagen, R. P. P. P. Grasman, and E. J. Wagenmakers, "A tutorial on fisher information," *J. Math. Psychol.*, vol. 80, pp. 40–55, Oct. 2017.
[69] M. Wei, A. Zhang, L. Qi, B. Li, and J. Sun, "An efficient frequency estimator for a complex exponential signal based on interpolation of selectable DTFT samples," *Sensors*, vol. 22, no. 3, p. 861, 2022.
[70] H. L. Van Trees, *Detection, Estimation, and Modulation Theory. Part 1 - Detection, Estimation, and Linear Modulation Theory*. New York, NY, USA: Wiley, 1968.
[71] R. L. Graham, D. E. Knuth, and O. Patashnik, *Concrete Mathematics: A Foundation for Computer Science*. 2nd ed. Reading, MA, USA: Addison-Wesley, 1994.

ISABEL GALLARDO-DUVAL was born in Barcelona, Spain. She received the B.Sc. degree in aerospace systems engineering and the M.Sc. degree in aerospace science and technology from the Universitat Politècnica de Catalunya (UPC) in 2023 and 2024, respectively. She is currently pursuing the Ph.D. degree jointly with the Space Communications Research Group, i2CAT Foundation and the Astronomy and Geomatics Research Group, UPC. Her main research interests include GNSS-free positioning technologies and emerging communication paradigms, including 5G/6G and nonterrestrial networks.

JOAN FRANCESC MUNOZ-MARTIN (Member, IEEE) received the B.Sc., M.Sc., and Ph.D. degrees in telecommunications engineering from the Universitat Politècnica de Catalunya (UPC)-BarcelonaTech, Barcelona, Spain, in 2014, 2017, and 2021, respectively. He joined the UPC NanoSat Lab in 2013, where he actively participated in the system and software development for the different satellite missions of the laboratory. He was involved in the European Space Agency programs BEXUS 19, Fly Your Satellite II, and the 3Cat-5/FSSCat Mission. He was the payload lead for the circular polarization GNSS-R experiment from the MOSAiC Campaign in the Arctic Sea. He was a Research Technologist with the Jet Propulsion Laboratory, serving as an Electrical Engineer with the Cold Atom Laboratory, onboard the International Space Station; contributing to the Goldstone Solar System Radar signal processing activities; and continuing his activities in microwave radiometry and polarimetric GNSS-R through SMAP-Reflectometry. He is currently the Director of Space Communications, i2CAT Foundation. His main research interests are on 6G technologies applied to nonterrestrial networks and integrated sensing and communications. He was a recipient of several the JPL Group Awards, one JPL Voyager Honor Award, and the NASA Group Award.

ADRIA ROVIRA-GARCIA (Senior Member, IEEE) is a Serra Hunter Associate Professor with the Department of Physics, Universitat Politecnica de Catalunya, Barcelona, Spain. He co-authored 40 papers in peer-reviewed journals, two book chapters, and over 50 works in meeting proceedings, with one best presentation award from the U.S. Institute of Navigation. His research interests are focused on high-accuracy navigation, integrity systems, ionospheric modeling, and scintillation.

JOAN A. RUIZ-DE-AZUA (Member, IEEE) was born in Barcelona, Spain. He received the first degree in aerospace engineering from Supaero, Toulouse, France, in 2015, the second degree in telecommunications engineering from the Universitat Politècnica de Catalunya (UPC), Barcelona, Spain, in 2015, the M.S. degree in network protocols from Supaero in 2015, and the Ph.D. degree in telecommunications engineering from UPC in 2020. He conducted his M.S. thesis about Avionic Full Duplex Switched Ethernet for critical networks with the École Polytéchnique de Montréal, Montreal, Canada. This dissertation contributes to the Internet of Satellites paradigm in which satellites from different stakeholders establish temporal and opportunistic Inter-Satellite Networks because remote satellites want to collaborate between them. For all his contributions, he was awarded the Cum Laude mention for the excellence of his Ph.D. dissertation. Furthermore, he has participated in five CubeSat missions in the five three years, highlighting the FSSCat mission, in which he participated as responsible for the FSS Experiment payload. This mission contributed to the Copernicus program with dedicated data on ice coverage and ice thickness. This mission was selected as the winner of the Copernicus Masters competition and the Sentinel Small Satellite challenge. His research interests are linked to satellite networks, non-terrestrial network architectures, disruptive tolerant routing protocols, application of artificial intelligence in satellite communications, integration of SDN/NFV in satellite constellations, the integration of IoT devices with satellite platforms, and quantum Internet.